

# A trace-regularized method for coherence retrieval\*

Chenglong Bao<sup>†</sup>, George Barbastathis<sup>‡</sup>, Hui Ji<sup>†</sup>, Zuowei Shen<sup>†</sup>, and Zhengyun Zhang<sup>§</sup>

**Abstract.** The mutual intensity and its equivalent phase-space representations quantify an optical field's state of coherence and are important tools in the study of light propagation and dynamics, but they can only be estimated indirectly from measurements through a process called coherence retrieval, otherwise known as phase-space tomography. As practical considerations often rule out the availability of a complete set of measurements, coherence retrieval is usually a challenging high-dimensional ill-posed inverse problem. In this paper, we propose a trace-regularized optimization model for coherence retrieval and a provably-convergent adaptive accelerated proximal gradient algorithm for solving the resulting problem. Applying our model and algorithm to both simulated and experimental data, we demonstrate an improvement in reconstruction quality over previous models as well as an increase in convergence speed compared to existing first-order methods.

**Key words.** phase-space tomography, trace regularization, accelerated proximal gradient method, adaptive restart

**AMS subject classifications.** 78M30, 78M50, 90C22

**1. Introduction.** *Coherence retrieval* is the unified mathematical treatment for two analogous physical measurement processes: estimating the density matrix of a quantum state, and reconstructing the mutual intensity of partially coherent light. Many, if not most coherence retrieval methods in optics originate from the seminal phase-space tomography approach [26, 20]. This reconstructed mutual intensity, or equivalent phase-space representations such as the Wigner distribution, is highly useful in that it can predict the three-dimensional distribution of light intensity after propagation through *any* known linear optical system [8, 16]. Likewise, knowledge of both the input and output coherence state of a system enables study of its dynamics [11]. Furthermore, the mutual intensity's phase-space representations enable intuitive understanding of light propagation [31] and form the physical basis for light field imaging in the field of computational photography [24, 23, 17, 39].

In a typical coherence retrieval experiment, stationary quasimonochromatic light in some unknown state of coherence is sent through one or more known optical systems, with the intensity measured at their outputs. The spatial coherence properties of this light source, *e.g.*, the mutual intensity, are then recovered from these measurements [32, 1, 4, 21, 18, 3, 26, 20, 14, 27, 33, 36, 34, 29]. More concretely, the electric field for quasimonochromatic light at position  $\mathbf{r}$  can be described by a complex-valued stochastic function  $U(\mathbf{r})$ . The mutual

---

\*Submitted to the editors April 3, 2017.

**Funding:** The work of the authors was partially supported by Singapore MOE Research Grant MOE2014-T2-1-065 and MOE2013-T3-1-008. The research was supported by the National Research Foundation (NRF), Prime Ministers Office, Singapore, under its CREATE programme, Singapore-MIT Alliance for Research and Technology (SMART) BioSystems and Micromechanics (BioSyM) IRG.

<sup>†</sup>Department of Mathematics, National University of Singapore ([matbc](mailto:matbc@nus.edu.sg), [matjh](mailto:matjh@nus.edu.sg), [matzuows@nus.edu.sg](mailto:matzuows@nus.edu.sg)).

<sup>‡</sup>Singapore-MIT Alliance for Research and Technology (SMART) Centre, and Department of Mechanical Engineering, Massachusetts Institute of Technology, ([gbarb@mit.edu](mailto:gbarb@mit.edu)).

<sup>§</sup>Singapore-MIT Alliance for Research and Technology (SMART) Centre, ([zhengyun@smart.mit.edu](mailto:zhengyun@smart.mit.edu)).

intensity is the correlation function describing this electric field, given by:

$$(1) \quad J(\mathbf{r}_1, \mathbf{r}_2) = \mathbb{E}[U(\mathbf{r}_1)U^*(\mathbf{r}_2)] = \iint v_1 v_2^* P_U(v_1, v_2; \mathbf{r}_1, \mathbf{r}_2) dv_1 dv_2,$$

where  $\mathbb{E}[\cdot]$  denotes the expected value (*i.e.*, the ensemble average),  $*$  denotes the complex conjugate, and  $P_U(v_1, v_2; \mathbf{r}_1, \mathbf{r}_2)$  is the joint probability density function for  $U(\mathbf{r}_1) = v_1$  and  $U(\mathbf{r}_2) = v_2$ . We choose some basis  $\{\xi_i\}_i$  and approximate the field as  $U(\mathbf{r}) = \sum_{i=1}^N u_i \xi_i(\mathbf{r})$  where  $\{u_i\}_i$  are complex-valued random variables. This naturally yields a discretization for the mutual intensity (1) as a Hermitian positive semidefinite matrix  $\mathbf{X} = \mathbb{E}(\mathbf{u}\mathbf{u}^H)$  such that

$$(2) \quad J(\mathbf{r}_1, \mathbf{r}_2) = \boldsymbol{\xi}^T(\mathbf{r}_1) \mathbf{X} \boldsymbol{\xi}^*(\mathbf{r}_2),$$

where  $\mathbf{u} = [u_1, u_2, \dots, u_N] \in \mathbb{C}^N$ , and  $\boldsymbol{\xi}(\mathbf{r}) = [\xi_1(\mathbf{r}), \xi_2(\mathbf{r}), \dots, \xi_N(\mathbf{r})]$ . The basis  $\{\xi_i\}_i$  can be sinc functions, Hermite functions or the prolate spheroidal functions, and they are chosen based on both ease of computation and efficiency in representing the field and mutual intensity. Given this discretization, the available measured intensities  $\{y_m\}_m$  can be expressed as:

$$(3) \quad y_m = \text{tr}(\mathbf{K}_m^H \mathbf{X}) + n_m,$$

where  $\text{tr}(\cdot)$  denotes the trace,  $^H$  denotes conjugate transpose,  $\mathbf{K}_m$  denotes the  $m$ th discretized measurement operator and  $n_m$  denotes the noise term. The  $\mathbf{K}_m$ s fully describe the propagation of light from the source to the measurement, and therefore they depend on the measurement procedure and discretization scheme; they are often specified as point-wise samples of a continuous function with an implicit assumption on the continuous quantities being spatially band-limited. See [subsection 2.1](#) for a derivation of the  $\mathbf{K}_m$ s based on physical first principles as well as an explicit form for the  $\mathbf{K}_m$ s in a typical phase-space tomography setup. The  $n_m$ s can be well-approximated by zero-mean normal distributions with standard deviations  $\sigma_m$ s if measurements are from a standard camera sensor pixel with at least  $\sim 10$  photons recorded and the noise level before quantization is much larger than a single quantization level.

The problem of coherence retrieval is then about recovering  $\mathbf{X}$  from the measured intensities  $\{y_m\}_m$ , which can be formulated as solving a weighted least-squares semidefinite problem:

$$(4) \quad \underset{\mathbf{X}}{\text{minimize}} \quad \sum_{m=1}^M \frac{1}{2\sigma_m^2} \left( \text{tr}(\mathbf{K}_m^H \mathbf{X}) - y_m \right)^2 \quad \text{subject to} \quad \mathbf{X} \in \mathcal{S}_+^N,$$

where  $\mathcal{S}^N$  is the set of  $N \times N$  Hermitian matrices,  $\mathcal{S}_+^N$  is the set of  $N \times N$  positive semidefinite matrices in  $\mathcal{S}^N$ , and  $M$  is the total number of measurements.

In practice, coherence retrieval is usually an ill-posed inverse problem. Recovering the  $N \times N$  coefficient matrix  $\mathbf{X}$  requires  $O(N^2)$  measurements and thus a measurement operator of size  $O(N^4)$ , which would require prohibitively high computational and storage costs. Furthermore, even with smaller values of  $N$ , sometimes it is not straight-forward to take enough measurements for the operator to have a reasonable condition number. For example, in lens-less phase-space tomography, the camera would need to be translated both infinitely far away and behind the source to capture a complete set of measurements.

To tackle these difficulties, one could introduce optical elements such as lenses [20, 19], but this can also introduce systematic error in the solution without accurate enough calibration of optical element positioning and aberrations. Another approach is to add a regularization term to (4); for example, nuclear norm regularization is used in [33] to promote low-rank solutions. However, the nuclear norm treats all spatial modes equally which might not be reasonable or flexible enough in many coherence retrieval scenarios in practice.

This paper aims to develop an effective reconstruction scheme for coherence retrieval. We propose a trace-regularized approach based on a penalty term proportional to the total intensity of light after passing through a chosen (virtual) linear system. The proposed regularization is motivated by the concept that for a set of solutions with similar likelihood, the one which is least energetic is likely to be closer to the truth—the extra intensity could simply be an artifact due to noise in the measurements, and this phenomenon is empirically observed in numerical experiments. This observation leads to the following trace-regularized optimization formulation for coherence retrieval:

$$(5) \quad \underset{\mathbf{X}}{\text{minimize}} \quad \sum_{m=1}^M \frac{1}{2\sigma_m^2} \left( \text{tr}(\mathbf{K}_m^H \mathbf{X}) - y_m \right)^2 + \mu \text{tr}(\mathbf{D}^H \mathbf{X}) \quad \text{subject to} \quad \mathbf{X} \in \mathcal{S}_+^N,$$

where  $\mu > 0$  is the penalty parameter and  $\mathbf{D} \in \mathcal{S}_+^N$  is a whitening matrix that boosts unlikely components in  $\mathbf{X}$  based on *a priori* information. Candidates for the matrix  $\mathbf{D}$  include difference operators or high-pass filters constructed from wavelet tight frames.

To solve the new model (5), we present an efficient first-order scheme, which is based on the accelerated proximal gradient (APG) method [6] with adaptive restart [25, 30]. Under some mild conditions on the measurement operators  $\mathbf{K}_m$ s, we prove that the proposed algorithm is globally convergent—the generated sequence converges to a global minimum of (5). Furthermore, we also propose a sufficient condition for when our algorithm is provably *linearly* convergent. Numerical results show the advantage of the proposed model with both simulated and experimental data. In addition, the proposed numerical algorithm also outperforms other state-of-the-art methods in terms of computational efficiency for these data sets.

The rest of the paper is organized as follows: we present our proposed coherence retrieval model in section 2, a numerical algorithm to solve the proposed model in section 3, its convergence analysis in section 4, numerical experiments for both simulated and experimental data in section 5, and a discussion of the results in section 6.

**2. The trace-regularized coherence retrieval model.** We will first introduce the measurement operators  $\mathbf{K}_m$ s and then present our trace-regularized model for coherence retrieval.

**2.1. Measurement operators.** In typical experimental conditions, light propagates linearly from a source point  $\mathbf{r}$  to one of the  $M$  measurement points  $\mathbf{r}_m$ , traversing various parts of an experimental apparatus. This linear relationship is characterized by the possibly stochastic kernel  $K(\mathbf{r}, \mathbf{r}_m)$ , known as the transmission function [8] or the amplitude spread function [16]:

$$U(\mathbf{r}_m) = \int U(\mathbf{r})K(\mathbf{r}, \mathbf{r}_m) d\mathbf{r}$$

The resulting intensity at point  $\mathbf{r}_m$  is the expected value of the magnitude of the electric field squared, yielding the Hopkins integral:

$$I(\mathbf{r}_m) = \mathbb{E}[U(\mathbf{r}_m)U^*(\mathbf{r}_m)] = \iint \mathbb{E}[U(\mathbf{r}_1)U^*(\mathbf{r}_2)] \mathbb{E}[K(\mathbf{r}_1, \mathbf{r}_m)K^*(\mathbf{r}_2, \mathbf{r}_m)] d\mathbf{r}_1 d\mathbf{r}_2$$

if we assume that the statistical fluctuations in the optical field are independent of the statistical fluctuations in  $K$ , which is typically the case in practical scenarios. Using the definition of the mutual intensity (1) as well as our discretization scheme (2), we obtain:

$$(6) \quad I(\mathbf{r}_m) = \iint \boldsymbol{\xi}^\top(\mathbf{r}_1) \mathbf{X} \boldsymbol{\xi}^*(\mathbf{r}_2) \mathbb{E}[K(\mathbf{r}_1, \mathbf{r}_m)K^*(\mathbf{r}_2, \mathbf{r}_m)] d\mathbf{r}_1 d\mathbf{r}_2$$

Now let us define a random vector  $\mathbf{k}_m \in \mathbb{C}^N$  with  $n$ th element  $\mathbf{k}_m[n] = \int \xi_n(\mathbf{r})K(\mathbf{r}, \mathbf{r}_m) d\mathbf{r}$  and probability density  $P_{\mathbf{k}_m}(\hat{\mathbf{k}}_m)$  for each realization  $\hat{\mathbf{k}}_m \in \mathbb{C}^N$ . Thus, we can define our discretized measurement operator as

$$(7) \quad \mathbf{K}_m = \mathbb{E}[\mathbf{k}_m^* \mathbf{k}_m^\top] = \int P_{\mathbf{k}_m}(\hat{\mathbf{k}}_m) \hat{\mathbf{k}}_m^* \hat{\mathbf{k}}_m^\top d\hat{\mathbf{k}}_m$$

to arrive at  $I(\mathbf{r}_m) = \text{tr}(\mathbf{K}_m^\text{H} \mathbf{X}) = y_m - n_m$ . In many situations, the  $\mathbf{K}_m$ s are low rank; for example, rank-one operators were used in [33, 38], and we will use them here as well. With these definitions, we now give an explicit form for the  $\mathbf{k}_m$ s, and hence the  $\mathbf{K}_m$ s, in the case of one-dimensional phase-space tomography based on axial translation; this measurement setup is what we will use in our numerical experiments.

**Example 2.1.** *In one-dimensional lensless phase-space tomography, the desired mutual intensity is of the form  $J(x_1, x_2)$  where  $x_1$  and  $x_2$  are both coordinates along the same axis of a reference plane (where we define  $z = 0$ ) and measurements are made at positions  $x_m$  in some plane located at location  $z_m$  along the direction of propagation. Supposing that the optical field can be Nyquist sampled at rate  $\Delta$  and has negligible energy for  $x < 0$  or  $x > N\Delta$ , then we can discretize the mutual intensity and the field using:*

$$\xi_n(x) = \sqrt{\Delta} \sin[\pi(x - n\Delta)/\Delta] / [\pi(x - n\Delta)].$$

Using the Fresnel diffraction formula for  $K$  and ignoring constant phase terms (with respect to  $x$ ), we obtain that

$$\begin{aligned} \mathbf{k}_m[n] &= \int \xi_n(x) \exp\left[\frac{i2\pi}{\lambda z_m}(x_m - x)^2\right] / \sqrt{i\lambda z_m} dx \\ &= \frac{\exp(\alpha_{m,n})}{2\sqrt{i\lambda z_m/\Delta}} \left\{ \text{erf}\left[-\sqrt{\alpha_{m,n}} + \frac{\sqrt{i\pi\lambda z_m}}{2\Delta}\right] - \text{erf}\left[-\sqrt{\alpha_{m,n}} - \frac{\sqrt{i\pi\lambda z_m}}{2\Delta}\right] \right\}, \end{aligned}$$

where  $i$  is the imaginary constant,  $\sqrt{i} = (1 + i)/\sqrt{2}$ ,  $\text{erf}(\zeta) = \frac{2}{\sqrt{\pi}} \int_0^\zeta \exp(-t^2) dt$  is the error function,  $\lambda$  is the wavelength of light and  $\alpha_{m,n} = i\pi(x_m - n\Delta)^2/(\lambda z_m)$ .

**2.2. The proposed model.** We propose regularization via the use of a penalty term proportional to  $\text{tr}(\mathbf{D}^H \mathbf{X})$ , where  $\mathbf{D}$  is some positive semidefinite matrix. More specifically, let us define a linear operator  $\mathcal{A} : \mathcal{S}^N \rightarrow \mathbb{R}^M$  whose  $m$ th element is  $\mathcal{A}(\mathbf{X})[m] = \text{tr}(\mathbf{K}_m^H \mathbf{X})/\sigma_m$  and the measurement vector  $\mathbf{b} \in \mathbb{R}^M$  whose  $m$ th element is  $\mathbf{b}[m] = y_m/\sigma_m$ . Then, we propose regularized coherence retrieval via the following convex problem:

$$(8) \quad \underset{\mathbf{X}}{\text{minimize}} \quad \frac{1}{2} \|\mathcal{A}(\mathbf{X}) - \mathbf{b}\|_2^2 + \mu \text{tr}(\mathbf{D}^H \mathbf{X}) \quad \text{subject to} \quad \mathbf{X} \in \mathcal{S}_+^N,$$

where  $\mu \geq 0$  is a weighting term for the regularizer and  $\mathbf{D} \in \mathcal{S}_+^N$ . The regularization term  $\text{tr}(\mathbf{D}^H \mathbf{X})$  in (8) is proportional to the intensity after propagation through some specific optical system. Note when  $\mathbf{D} = \mathbf{I}$ , this regularization term is proportional to the total energy in the source, as if we used a large enough single element sensor to capture all of the photons emitted from the source. This case also coincides with the nuclear norm regularization proposed in [33] for a low-rank assumption on  $\mathbf{X}$ , since  $\mathbf{X} \in \mathcal{S}_+^N$ . However, we arrive at this regularizer from an alternative perspective, and the flexibility of choosing a  $\mathbf{D}$  other than identity enables us to more effectively incorporate *a priori* information regarding  $\mathbf{X}$ .

Our motivation for using the trace is based on the following observation. Suppose we wish to reconstruct some true matrix  $\mathbf{X}_\star$  from measurements  $\mathbf{b} = \mathcal{A}(\mathbf{X}_\star) + \mathbf{n}$ , where  $\mathbf{n} \sim \mathcal{N}(\mathbf{0}, \sigma^2 \mathbf{I})$  and  $\mathcal{A}$  is an ideal linear operator, *i.e.*,  $\mathcal{A}^H \mathcal{A}$  is identity. The probability distribution for the least squares estimator<sup>1</sup> would be Gaussian with mean  $\mathbf{X}_\star$ , and the positive semidefinite least squares estimator<sup>2</sup> would be distributed similarly, except with values outside  $\mathcal{S}_+^N$  projected onto  $\mathcal{S}_+^N$ . This projection elevates negative eigenvalues to zero, and thus an easily observable side effect is that the expected value of the trace of the positive semidefinite least squares estimator is higher than the trace of  $\mathbf{X}_\star$ . Furthermore, for a  $\mathbf{X}_\star$  with many small eigenvalues, it is very likely for noise to introduce negative eigenvalues in the least squares estimator, which are then corrected by the semidefinite constraint. Errors which do not result in negative eigenvalues are *not* corrected by this constraint. Hence, this asymmetry makes the trace a good predictor of reconstruction error  $\|\mathbf{X} - \mathbf{X}_\star\|_F$ .

We can see this effect explicitly through simulated measurements of a Gaussian Schell-model source [28] (with parameter  $\beta = 1$ ). In this numerical experiment, we choose for simplicity the Hermite functions  $\phi_n(x)$  given in [28] as our spatial basis, and set  $\mathbf{X}_\star \in \mathcal{S}_+^N$  to be a diagonal  $32 \times 32$  matrix whose  $n$ th element is equal to  $2^{n-1} (3 + \sqrt{5})^{1-n}$ . Running this experiment 256 times for varying amounts of noise leads to the results shown in Figure 1 (a), where we observe the trace of the reconstructed  $\mathbf{X}$  being consistently higher than the true trace, with the trace tracking the general trend of reconstruction error as the noise level increases. The predictive power of the trace is shown in Figure 1 (b), where we see a positive correlation between the trace of the reconstruction and the reconstruction error. If we employ a  $\text{tr}(\mathbf{X})$  penalty term (*i.e.*,  $\mathbf{D} = \mathbf{I}$ ) in this reconstruction process, it is possible to arrive at a lower error reconstruction with judicious selection of  $\mu$ , as can be seen in Figure 1 (c).

However, by not setting  $\mathbf{D}$  to be the identity matrix, we can achieve even better performance, as can be seen in Figure 1 (c) with the use of a derivative operator. These gains stem

<sup>1</sup> $\arg \min_{\mathbf{X}} \frac{1}{2} \|\mathcal{A}(\mathbf{X}) - \mathbf{b}\|_2^2$

<sup>2</sup> $\arg \min_{\mathbf{X}} \frac{1}{2} \|\mathcal{A}(\mathbf{X}) - \mathbf{b}\|_2^2$  subject to  $\mathbf{X} \in \mathcal{S}_+^N$

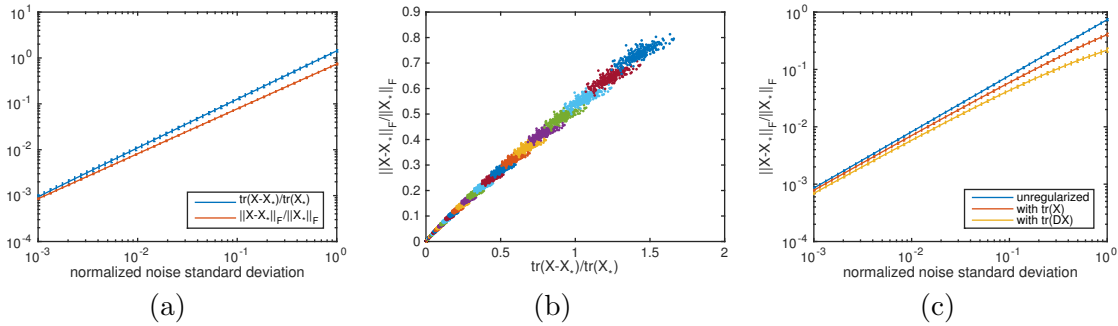


**Figure 1.** The effect of noise on the normalized trace difference as well as the normalized reconstruction error is shown in (a); the mean value across 256 trials is plotted with error bars indicating one standard deviation. Each trial is plotted as a point in a scatter plot of reconstruction error versus trace difference in (b), with each color representing trials for a specific level of noise. The effect of regularization on the average reconstruction error is shown in (c), where  $\mathbf{D}$  effectively applies a first order derivative operator to both coordinates in the original mutual intensity function, and optimal regularizer weighting values  $\mu$  are picked for each noise level.

from the application of *a priori* information about  $\mathbf{X}$ —since we are reconstructing Gaussian Schell-model sources, higher order modes are less likely than lower order modes. Thus, if we only used  $\text{tr}(\mathbf{X})$  as a penalizer, then a solution with energy concentrated in higher order modes would be penalized the same as a solution with energy concentrated in lower order modes as long as the total energy were the same, despite the fact that the latter would be more likely according to our *a priori* information. Hence, the introduction of  $\mathbf{D}$  enabled us apply this information, by elevating the “cost” of a higher order mode through the derivative operator, which amplifies the higher frequency components in the high order modes.

In typical scenarios, we often have at least some *a priori* information available to us. For example, the statistics of natural images suggest a decay property in amplitude of the Fourier transform of the intensity [9, 15, 35], meaning that naturally occurring optical fields will be more likely to have lower energy content in the higher spatial frequencies; this suggests setting  $\mathbf{D}$  as effectively a filter that boosts high frequency components. In this paper, we obtain good results from the use of simple matrices for  $\mathbf{D}$  such as one based on extracting the high-pass component using the Haar wavelet, whereas a more powerful and flexible approach would be to design  $\mathbf{D}$  based on the concept of high-pass filters of wavelet tight frames [13], which has been shown to have a close relationship to the difference operators [10].

**3. Numerical algorithm.** We will now briefly review the accelerated proximal gradient (APG) method [6] and then present a novel restart condition for solving (8).

**3.1. The accelerated proximal gradient method.** Define

$$(9) \quad f(\mathbf{X}) = \frac{1}{2} \|\mathcal{A}(\mathbf{X}) - \mathbf{b}\|_2^2 + \mu \langle \mathbf{D}, \mathbf{X} \rangle, \quad g(\mathbf{X}) = \iota_{\mathcal{S}_+^N}(\mathbf{X})$$

where  $\langle \mathbf{A}, \mathbf{B} \rangle = \text{tr}(\mathbf{A}^H \mathbf{B})$  is the inner product and  $\iota_{\mathcal{S}_+^N}(\cdot)$  is the indicator function for the set of positive semidefinite Hermitian matrices, *i.e.*,  $\iota_{\mathcal{S}_+^N}(\mathbf{X}) = 0$  if  $\mathbf{X} \in \mathcal{S}_+^N$  and  $\iota_{\mathcal{S}_+^N}(\mathbf{X}) = +\infty$  if  $\mathbf{X} \notin \mathcal{S}_+^N$ . Then, equation (8) is equivalent to the composite convex minimization problem

$$(10) \quad \underset{\mathbf{X} \in \mathcal{S}_+^N}{\text{minimize}} \quad h(\mathbf{X}) = f(\mathbf{X}) + g(\mathbf{X}).$$

One representative method to solve (10) is the so-called accelerated proximal gradient (APG) method [6]. Given a function  $g$  and  $\alpha > 0$ , define the proximal operator of  $g$  as

$$\text{Prox}_g^\alpha(\mathbf{X}) = \arg \min_{\mathbf{Y}} \left\{ g(\mathbf{Y}) + \frac{1}{2\alpha} \|\mathbf{Y} - \mathbf{X}\|_{\text{F}}^2 \right\}$$

where  $\|\cdot\|_{\text{F}}$  is the Frobenius norm. Then, the APG method constructs two sequences  $\{\mathbf{X}_k\}$  and  $\{\mathbf{Y}_k\}$  via the following steps:

$$(11a) \quad t_k = \left( \sqrt{4(t_{k-1})^2 + 1} + 1 \right) / 2,$$

$$(11b) \quad \mathbf{Y}_k = \mathbf{X}_k + \frac{t_{k-1}-1}{t_k} (\mathbf{X}_k - \mathbf{X}_{k-1}),$$

$$(11c) \quad \mathbf{X}_{k+1} = \text{Prox}_g^{\alpha_k}(\mathbf{Y}_k - \alpha_k \nabla f(\mathbf{Y}_k)),$$

where  $t_0 = 1$ ,  $0 < \alpha_k \leq 1/L$ , and  $L$  is the maximal eigenvalue of  $\mathcal{A}^H \mathcal{A}$  with  $\mathcal{A}^H$  being the adjoint operator for  $\mathcal{A}$ . With  $\mathcal{X}_\star$  being the set of minimizers of (10) and  $h_\star$  being the minimal value, it is well known that the APG method has the following convergence property [6]:

**Theorem 3.1.** *Let  $\mathbf{X}_k$  be the sequence generated by (11a)-(11c) and  $\alpha_k = 1/L, \forall k$ . Then for any  $k \geq 1$*

$$(12) \quad h(\mathbf{X}_k) - h_\star \leq \frac{2L \text{dist}(\mathbf{X}_0, \mathcal{X}_\star)^2}{(k+1)^2},$$

where  $\text{dist}(\mathbf{X}, \mathcal{X}_\star) = \inf \{ \|\mathbf{X} - \mathbf{Y}\|_{\text{F}} : \mathbf{Y} \in \mathcal{X}_\star \}$ .

**3.2. The proposed algorithm.** Indeed, the attractive  $O(1/k^2)$  convergence rate of the APG method is optimal when solving a convex problem when only first order information is available [22]. However, it has been observed that the objective value (the value of  $f$  in this case) sequence generated by the APG method shows oscillations, which slows down convergence speed in practice [25]. To avoid these oscillations, restarting techniques were proposed in [25] wherein  $t_k$  is reset to 1 when certain criteria are met. Despite the numerical success of this adaptive restart APG method, it is still unknown whether this method is guaranteed to converge. We therefore propose a new restart criterion that leads to a globally convergent numerical algorithm for solving the trace-regularized coherence retrieval problem (8). Given per-iteration step size  $\alpha_k > 0$ , define

$$(13) \quad \mathbf{Z}_{k+1} = \text{Prox}_g^{\alpha_k}(\mathbf{Y}_k - \alpha_k \nabla f(\mathbf{Y}_k)), \quad \mathbf{U}_k = \mathbf{Y}_k - \mathbf{Z}_{k+1}, \quad \mathbf{V}_k = \mathbf{X}_k - \mathbf{Z}_{k+1}.$$

We restart our APG method by setting  $t_k = 1$  if the following inequality does not hold:

$$(14) \quad \langle \mathbf{U}_k, \mathbf{V}_k \rangle - \alpha_k \langle \mathcal{A}(\mathbf{U}_k), \mathcal{A}(\mathbf{V}_k) \rangle \geq \gamma \|\mathbf{V}_k\|_{\text{F}}^2$$

where  $\gamma > 0$  is a small constant. We note that no extra computation is needed for checking criterion (14) due to the linearity of  $\mathcal{A}$  and the necessary quantities having been computed either during step size estimation or in a previous iteration. We summarize our proposed adaptive APG algorithm in [Algorithm 1](#).

**Algorithm 1** Adaptive APG algorithm

---

```

1: Initialize  $\mathbf{X}_1 = \mathbf{Y}_1 = \mathbf{Y}_0 = \mathbf{X}_0$ ,  $t_1 = 1$ ,  $k_{\max}, k_{\max\text{res}} \in \mathbb{N}$ ,  $k = 1$ ,  $k_{\text{res}} = 0$ , and  $\rho \in (0, 1)$ 
2: while  $k < k_{\max}$  do
3:   Estimate step size  $\alpha_k$  using Algorithm 2 and obtain  $\mathbf{Z}_{k+1} = \text{Prox}_g^{\alpha_k}(\mathbf{Y}_k - \alpha_k \nabla f(\mathbf{Y}_k))$ .
4:   if (14) holds and  $k - k_{\text{res}} \leq k_{\max\text{res}}$  then
5:     Set  $\mathbf{X}_{k+1} = \mathbf{Z}_{k+1}$ .
6:     Set  $t_{k+1} = \frac{1}{2} \left( \sqrt{4t_k^2 + 1} + 1 \right)$ .
7:     Set  $\mathbf{Y}_{k+1} = \mathbf{X}_{k+1} + \frac{t_k - 1}{t_{k+1}} (\mathbf{X}_{k+1} - \mathbf{X}_k)$ .
8:     Set  $k = k + 1$ .
9:   else
10:    Reset  $t_k = 1$  and update  $k_{\text{res}} = k$ .
11:    Set  $\mathbf{Y}_k = \mathbf{X}_k$ .
12:   end if
13: end while

```

---

**3.2.1. Step size estimation.** Setting  $\alpha_k = 1/L$  might be too conservative when the Lipschitz constant  $L$  is large. We would like to adaptively choose  $\alpha_k$  by first initializing with the Barzilai-Borwein (BB) method [5]; our choice of the form with the squared norm in the denominator is motivated by numerical considerations—an inner product is sensitive to cancellation errors and placing it in the denominator can result in numerical instability. After initialization, we then use a standard backtracking technique and adopt the step size  $\alpha_k$  at  $\mathbf{Y}_k$  whenever the following inequality holds:

$$(15) \quad h(\mathbf{Y}_k) - h(\mathbf{Z}_{k+1}) \geq \delta \|\mathbf{Y}_k - \mathbf{Z}_{k+1}\|_F^2,$$

where  $\delta > 0$  is a small constant. It is noted that (15) holds whenever  $\alpha_k \leq 1/(L + \delta)$  and hence backtracking must terminate. In practice, we find that BB initialization gives a good estimate for the step size and that backtracking is rare. A detailed listing for this step size estimation algorithm is given in [Algorithm 2](#).

**4. Convergence analysis.** In this section, we focus on convergence analysis for [Algorithm 1](#) including an analysis regarding global convergence as well as on the convergence rate. Before proceeding, we first introduce some notation and definitions to be used in the analysis.

**4.1. Notation and definitions.** Denote  $\mathcal{X}_*$  to be the solution set of (8). Given a point  $\mathbf{x}$  and  $\epsilon > 0$ , we define  $\mathbb{B}(\mathbf{x}, \epsilon) = \{\mathbf{y} : \|\mathbf{x} - \mathbf{y}\|_2 \leq \epsilon\}$ . Given a set  $\mathcal{X}$ , the relative interior of  $\mathcal{X}$ , denoted by  $\text{ri}(\mathcal{X})$ , is defined as

$$\text{ri}(\mathcal{X}) := \{\mathbf{x} \in \mathcal{X} : \exists \epsilon > 0, \mathbb{B}(\mathbf{x}, \epsilon) \cap \text{aff}(\mathcal{X}) \subseteq \mathcal{X}\},$$

where  $\text{aff}(\mathcal{X})$  is the affine hull of  $\mathcal{X}$ . Given a set  $\mathcal{X}$  and a member  $\mathbf{x}$ , the distance from  $\mathbf{x}$  to  $\mathcal{X}$ , denoted by  $\text{dist}(\mathbf{x}, \mathcal{X})$ , is defined as  $\text{dist}(\mathbf{x}, \mathcal{X}) = \inf \{\|\mathbf{x} - \mathbf{y}\|_2 : \mathbf{y} \in \mathcal{X}\}$ . Given a function  $f$  and  $b \in \mathbb{R}$ , we define the sub-level set  $[f(\mathbf{x}) \leq b]$  to be  $\{\mathbf{x} : f(\mathbf{x}) \leq b\}$ . We use  $\partial f$  to denote the (limiting) subgradient of  $f$ .

**Algorithm 2** Estimation of step size  $\alpha_k$ 


---

```

1: Inputs:  $\mathbf{Y}_k, \mathbf{Y}_{k-1}, \nabla f(\mathbf{Y}_k), \nabla f(\mathbf{Y}_{k-1}), \rho < 1$  and  $\alpha_{\min}, \alpha_{\max} > 0$ .
2: Outputs: Step size  $\alpha_k$ , proximal point  $\mathbf{Z}_{k+1}$ 
3: if  $k=1$  then
4:   Initialize  $\beta = \|\mathbf{b} - \mathcal{A}(\mathbf{Y}_k)\|_{\mathbb{F}}^2 / \|\mathcal{A}^H[\mathbf{b} - \mathcal{A}(\mathbf{Y}_k)]\|_{\mathbb{F}}^2$ .
5: else
6:   Calculate  $\mathbf{S}_k = \mathbf{Y}_k - \mathbf{Y}_{k-1}$  and  $\mathbf{T}_k = \nabla f(\mathbf{Y}_k) - \nabla f(\mathbf{Y}_{k-1})$ .
7:   Initialize  $\beta = |\langle \mathbf{S}_k, \mathbf{T}_k \rangle| / \|\mathbf{T}_k\|_{\mathbb{F}}^2$ .
8: end if
9: for  $j = 1, 2 \dots$  do
10:  Calculate  $\mathbf{Z}_{k+1} = \text{Prox}_g^\beta[\mathbf{Y}_k - \beta \nabla f(\mathbf{Y}_k)]$ .
11:  if the inequality (15) holds or (14) fails to hold or  $\beta < \alpha_{\min}$  then
12:    break
13:  else
14:    Backtrack  $\beta = \rho\beta$ .
15:  end if
16: end for
17: Set  $\alpha_k = \min[\max(\alpha_{\min}, \beta), \alpha_{\max}]$ .

```

---

Let  $\mathcal{A}$  and  $\mathcal{B}$  be finite dimensional Euclidean spaces and  $\Gamma : \mathcal{A} \rightrightarrows \mathcal{B}$  be a *set-valued mapping*. The *graph*, *domain* and *inverse* of  $\Gamma$  are defined by

$$\text{gph}(\Gamma) := \{(\mathbf{u}, \mathbf{v}) : \mathbf{v} \in \Gamma(\mathbf{u})\}, \quad \text{dom}(\Gamma) := \{\mathbf{u} : \Gamma(\mathbf{u}) \neq \emptyset\}, \quad \Gamma^{-1}(\mathbf{v}) := \{\mathbf{u} : \Gamma(\mathbf{u}) = \mathbf{v}\}.$$

In the following context, we define a useful property for set-valued mappings.

**Definition 4.1.** A set-valued mapping  $\Gamma : \mathcal{A} \rightrightarrows \mathcal{B}$  is said to be *metrically subregular* at  $\bar{\mathbf{x}} \in \mathcal{A}$  for  $\bar{\mathbf{y}} \in \mathcal{B}$  if  $(\bar{\mathbf{x}}, \bar{\mathbf{y}}) \in \text{gph}(\Gamma)$  and there exist  $\kappa, \epsilon > 0$  such that

$$(16) \quad \text{dist}(\mathbf{x}, \Gamma^{-1}(\bar{\mathbf{y}})) \leq \kappa \text{dist}(\bar{\mathbf{y}}, \Gamma(\mathbf{x})), \quad \forall \mathbf{x} \in \mathbb{B}(\bar{\mathbf{x}}, \epsilon).$$

**4.2. Global convergence.** We first show that [Algorithm 1](#) converges to a global minimum, provided the generated sequence is bounded.

**Theorem 4.2.** Let  $\{\mathbf{X}_k\}$  be the sequence generated by [Algorithm 1](#). If  $\{\mathbf{X}_k\}$  is bounded, then  $\{\mathbf{X}_k\}$  converges to a global minimum of (8), denoted as  $\bar{\mathbf{X}}$ .

*Proof.* See Appendix A. ■

**Remark 4.1.** The proof is based on the recently established Kurdyka-Lojasiewicz (KL) property [2, 7], which provides a framework for typical descent algorithms whose generated sequences are bounded. However, the boundedness condition might not hold for semidefinite programming problems such as (8).

In coherence retrieval, we will show that the boundedness condition on  $\{\mathbf{X}_k\}$  holds when the measurement operator  $\mathcal{A}$  satisfies certain mild condition. Let  $\mathbf{A} = (\hat{\mathbf{K}}_1, \dots, \hat{\mathbf{K}}_M)^H \in \mathbb{C}^{MN \times N}$  where the  $\hat{\mathbf{K}}_m \in \mathbb{C}^{N \times N}$  are such that  $\mathbf{K}_m = \hat{\mathbf{K}}_m \hat{\mathbf{K}}_m^H$  for all  $m \in \{1, \dots, M\}$ . We make the following assumption on  $\mathbf{A}$ :

**Assumption 4.1.** *The matrix  $\mathbf{A}$  has full column rank.*

In practice, [Assumption 4.1](#) always holds because either the measurements are designed to ensure  $\mathbf{A}$  is full rank, or a smaller set of basis functions are used to remove the ambiguity, e.g., we can choose a larger sampling interval in the case of sinc basis functions, or we can use the nonzero right singular vectors of  $\mathbf{A}$  to set a new basis based on our original basis.

**Proposition 4.1.** *Let  $\{\mathbf{X}_k\}$  to be the sequence generated by [Algorithm 1](#). Suppose [Assumption 4.1](#) holds. Then,  $\{\mathbf{X}_k\}$  is bounded.*

*Proof.* See [Appendix B](#). ■

Combining [Theorem 4.2](#) and [Proposition 4.1](#), we obtain that [Algorithm 1](#) is globally convergent under [Assumption 4.1](#).

**Corollary 4.1.** *Let  $\{\mathbf{X}_k\}$  to be the sequence generated by [Algorithm 1](#). Suppose [Assumption 4.1](#) holds. Then,  $\{\mathbf{X}_k\}$  converges to a global minimum of (8), denoted as  $\bar{\mathbf{X}}$ .*

**4.3. Convergence rate analysis.** In this section, we first impose a reasonable condition on the solution set  $\mathcal{X}_*$ . Using this condition, we prove that [Algorithm 1](#) converges linearly.

**Assumption 4.2.** *We make the following assumptions on  $\mathcal{X}_*$ : a)  $\mathcal{X}_* \neq \emptyset$ . b) There exists an  $\mathbf{X}_* \in \mathcal{X}_*$  satisfying*

$$(17) \quad \mathbf{0} \in \nabla f(\mathbf{X}_*) + \text{ri}\left(\mathcal{N}_{\mathcal{S}_+^N}(\mathbf{X}_*)\right)$$

where  $\mathcal{N}_{\mathcal{S}_+^N}(\mathbf{X})$  denotes the normal cone of  $\mathcal{S}_+^N$  at  $\mathbf{X}$ .

**Remark 4.2.** *The first order optimality condition of  $h$  implies*

$$(18) \quad \mathbf{0} \in \nabla f(\mathbf{X}) + \mathcal{N}_{\mathcal{S}_+^N}(\mathbf{X}), \quad \forall \mathbf{X} \in \mathcal{X}_*.$$

Condition (17) is slightly more restrictive than (18), but (17) only needs to hold at one point of  $\mathcal{X}_*$ . Moreover, from the proof of [Proposition 4.2](#), one sufficient condition for ensuring (17) is that there exists some  $\mathbf{X}_* \in \mathcal{X}_*$  such that  $\text{rank}(\mathbf{X}_*) = N$ , i.e.,  $\mathbf{X}_*$  is full rank.

Based on recent work [12], we ensure  $\partial h$  is metrically sub-regular at any  $\bar{\mathbf{X}} \in \mathcal{X}_*$  for  $\mathbf{0}$  in the next proposition.

**Proposition 4.2.** *Let  $h = f + g$  be defined in (9). Suppose [Assumption 4.2](#) holds. Then, for any  $\bar{\mathbf{X}} \in \mathcal{X}_*$ ,  $\partial h$  is metrically sub-regular at  $\bar{\mathbf{X}}$  for  $\mathbf{0}$ .*

*Proof.* See [Appendix C](#). ■

**Remark 4.3.** *Proposition 3.2 in [12] is a characterization of metric sub-regularity for real symmetric positive semidefinite matrices. However, the analysis in [12] can easily be extended for Hermitian positive semidefinite matrices over  $\mathbb{R}$ .*

Now, we can establish local linear convergence for [Algorithm 1](#) via the following:

**Theorem 4.3.** *Let  $h = f + g$  be defined in (9) and the sequence  $\{\mathbf{X}_k\}$  be generated by [Algorithm 1](#). Suppose [Assumption 4.1](#) and [Assumption 4.2](#) holds. Then, there exists some  $\bar{\mathbf{X}} \in \mathcal{X}_*$  such that one of the following assertions holds:*

1.  $\{\mathbf{X}_k\}$  converges to  $\bar{\mathbf{X}}$  in finite steps.
2.  $\{h(\mathbf{X}_k)\}$  and  $\{\mathbf{X}_k\}$  linearly converge to  $h(\bar{\mathbf{X}})$  and  $\bar{\mathbf{X}}$ , respectively, i.e., there exist  $c_1, c_2 > 0$ ,  $w_1, w_2 \in (0, 1)$  and  $k_\ell > 0$  such that

$$h(\mathbf{X}_k) - h(\bar{\mathbf{X}}) \leq c_1 w_1^k, \text{ and } \|\mathbf{X}_k - \bar{\mathbf{X}}\|_F \leq c_2 w_2^k, \forall k > k_\ell.$$

*Proof.* See [Appendix D](#). ■

**5. Results.** We now apply our algorithm to two sets of phase-space tomography data. One is a simulation with realistic noise of two coherent Gaussian beams that are slightly decohered with respect to each other. Another is experimental data from [38] consisting of a Schell-model source imaged by a single positive lens. In both cases, the data consists of intensity profiles captured at 250  $\mu\text{m}$  axial intervals by a 3.2  $\mu\text{m}$  pitch camera, and we use the discretization and forward model (i.e., the  $\xi_{ns}$  and  $\mathbf{K}_{ms}$ ) given in [Example 2.1](#), with wavelength  $\lambda$  equal to 532 nm. The constant parameters we chose for our numerical algorithm were:

$$(19) \quad \begin{array}{llll} \mathbf{X}_0 = \mathbf{0} & \delta = 10^{-8} & \gamma = 10^{-5} & \rho = \frac{1}{2} \\ \alpha_{\min} = 10^{-8} & \alpha_{\max} = 10^8 & k_{\max} = 1000 & k_{\text{resmax}} = 250 \end{array}$$

All computations were performed using MATLAB running on an Intel Xeon E5-2630 CPU.

**5.1. Simulated Data.** We simulate a mostly coherent sum of two parallel Gaussian beams with coplanar waists, as given by the following mutual intensity function:

$$(20) \quad \begin{aligned} J(x_1, x_2) = & \exp\left[-\frac{(x_1 - x_0)^2 + (x_2 - x_0)^2}{2\sigma^2}\right] + \exp\left[-\frac{(x_1 + x_0)^2 + (x_2 + x_0)^2}{2\sigma^2}\right] \\ & + \chi \left\{ \exp\left[-\frac{(x_1 - x_0)^2 + (x_2 + x_0)^2}{2\sigma^2}\right] + \exp\left[-\frac{(x_1 + x_0)^2 + (x_2 - x_0)^2}{2\sigma^2}\right] \right\} \end{aligned}$$

where  $x_0 = 64 \mu\text{m}$ ,  $\sigma = 32 \mu\text{m}$  and  $\chi = 0.9$ . This partially coherent field, discretized into a  $51 \times 51$  mutual intensity matrix using a sampling interval of 6.4  $\mu\text{m}$ , is then propagated to 201 axial positions spaced 250  $\mu\text{m}$  apart. For each axial position, we consider 101 intensity point samples spaced 3.2  $\mu\text{m}$  apart for the measurements. This set of true intensities is shown in [Figure 2](#) under the heading “noiseless”. The smallest and largest singular values of matrix  $\mathbf{A}$  as it is defined in [subsection 4.2](#) were  $a_{\min} = 3.094$  and  $a_{\max} = 7.925$ , respectively.

To emulate real world conditions where the  $\sigma_{ms}$  are unknown, we simulate collecting 16 measurements for each intensity point sample, with their mean treated as the  $y_{ms}$  in our model and the standard deviation across these 16 samples used as an approximation to  $\sigma_m \sqrt{16}$ . The noisy data for each measurement is generated by first drawing from a Poisson distribution whose rate parameter is proportional to the true intensity at that point, with the sum of all the rate parameters made to equal  $1.02 \times 10^5$  photons. We then add Gaussian noise with standard deviation equal to 0.01 times the maximum of all the rate parameters; this is to simulate readout and quantization noise that would be typically expected of an 8-bit sensor. This set of simulated measurements is shown in [Figure 2](#) under the heading “noisy”. We then run our algorithm with the following inputs:

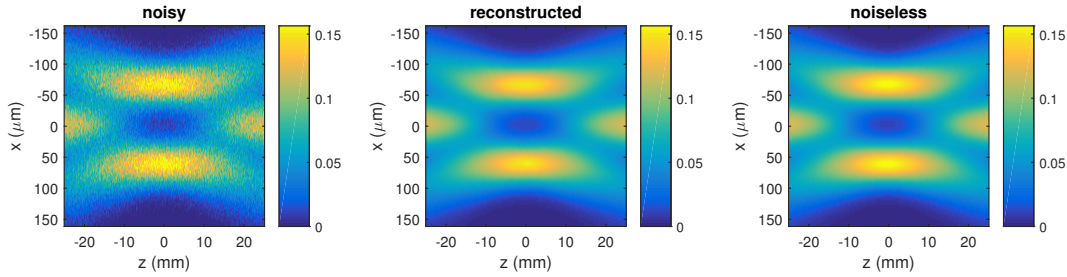


**Figure 2.** Noisy measurements of the intensity are shown on left, with the true intensity shown on right. Propagated intensity of a regularized reconstructed result is shown in center. In all images, light propagates from left to right, and the intensity is in arbitrary units.

- **noiseless:** The  $y_m$ s are set to the ideal noiseless intensity, with the  $\sigma_m$ s set to 1 and  $\mu = 0$  (*i.e.*, no regularization).
- **unregularized:** The  $y_m$ s and  $\sigma_m$ s are set to our simulated noisy data, with  $\mu = 0$  (*i.e.*, no regularization).
- **early stop:** This is the same as the unregularized case, except we terminate our algorithm when  $\frac{1}{2}\|\mathcal{A}(\mathbf{X}) - \mathbf{b}\|_2^2$  drops below  $\alpha M/2$  where  $\alpha = 1.5$ .
- **nuclear:** This uses the simulated noisy data and lets  $\mathbf{D} = \mathbf{I}$  (*i.e.*, nuclear norm regularization).  $\mu$  is set such that  $\frac{1}{2}\|\mathcal{A}(\mathbf{X}) - \mathbf{b}\|_2^2 \approx \alpha M/2$  upon convergence.
- **gradient:** This uses the simulated noisy data and lets  $\mathbf{D}$  be a tridiagonal matrix with all the elements in the diagonal equal to 1 and all the off-diagonal elements equal to  $-\frac{1}{2}$ .  $\mu$  is set such that  $\frac{1}{2}\|\mathcal{A}(\mathbf{X}) - \mathbf{b}\|_2^2 \approx \alpha M/2$  upon convergence.

The  $\alpha M/2$  threshold for  $\frac{1}{2}\|\mathcal{A}(\mathbf{X}) - \mathbf{b}\|_2^2$  arises from the fact that the norm-squared expression follows a chi-squared distribution with  $M$  degrees of freedom assuming that the  $\sigma_m$ s are correct values for the standard deviations of the Gaussian noise.  $M/2$  would be the mean for such a distribution, and  $\alpha$  is used to adjust the threshold to take into account how well estimated the  $\sigma_m$ s are and how much of the distribution we want to include. For this particular set of data, we are fairly confident of our estimates of  $\sigma_m$  and have thus set  $\alpha = 1.5$ . The **early stop** result is used as a point of reference for comparison with the regularized results, since these results all have approximately the same level of measurement mismatch, and therefore the differences are due to the presence of and choice of regularizer. The **gradient** penalty term  $\text{tr}(\mathbf{D}^H \mathbf{X})$  is equivalent to applying a Haar wavelet to both the rows and columns of  $\mathbf{X}$ , keeping only the high frequency components and then taking the trace. The application of  $\mathbf{D}$  is a simple approximation for a derivative operator on  $x_1$  and  $x_2$  in the continuous domain, and it physically corresponds to a desire to reduce the energy present in the first order spatial derivative of the optical wave function. Mathematically, it penalizes nonsmooth solutions to our problem, and it is motivated by our *a priori* knowledge that the true solution is smooth.

For comparison, we also run standard proximal gradients (PG), accelerated proximal gradients (APG) and adaptive restart accelerated proximal gradients (restart APG) on the **gradient** input, using publicly available code accompanying [25]. For instrumentation, we added code to the official source code in order to record the time taken and acceleration parameter at each iteration. Furthermore, each algorithm was run a second time wherein the

value of  $\mathbf{X}$  at each iteration was recorded in order to compute the value of the merit function at each iteration.

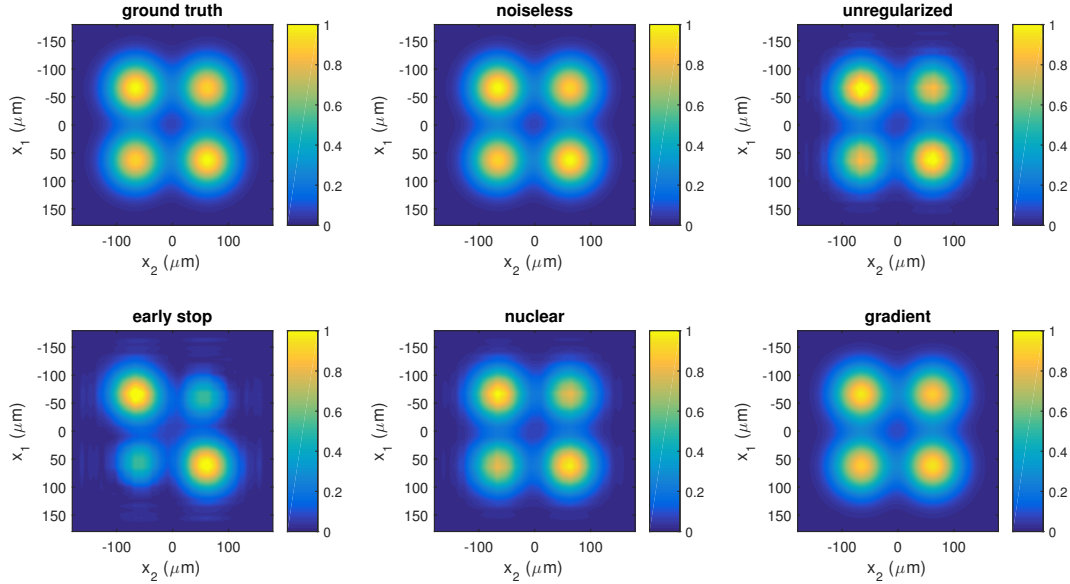


**Figure 3.** Magnitude of the mutual intensity functions for the simulated data. They are all drawn using the same scale, normalized to the maximum magnitude of the ground truth.

	noiseless	unregularized	early stop	nuclear	gradient
normalized RMSE	$7.524 \times 10^{-5}$	0.1147	0.3977	0.1438	0.039 79
trace distance	$6.103 \times 10^{-5}$	0.079 08	0.2887	0.076 58	0.025 34

**Table 1**

Quantitative measurements of error for the different reconstructed mutual intensity matrices. The normalized root mean square error (RMSE) is defined as  $\|\mathbf{X} - \mathbf{X}_{true}\|_F / \|\mathbf{X}_{true}\|_F$ . The trace distance, a quantity used to describe the difference between two quantum states, is equal to half the sum of the singular values of  $\rho - \rho_{true}$ , where  $\rho$  and  $\rho_{true}$  are trace-normalized versions of  $\mathbf{X}$  and  $\mathbf{X}_{true}$ , i.e., divided by their trace.

The magnitude of the reconstructed mutual intensity functions are shown in Figure 3, and the amplitude of their coherent modes [37] (they correspond to the eigenvectors of  $\mathbf{J}$  scaled by the square root of their eigenvalues) are given in Figure 4. The propagated intensity using the **gradient** result is shown in Figure 2. Since the ground truth is known, we give a summary of the reconstruction error using various metrics in Table 1. A convergence comparison between algorithms for the **gradient** input is shown in Figure 5.

As is evident from the results, especially Figure 4, noise introduces additional energy (as seen in the increased amplitude for the second mode) as well as an additional mode, resulting in a reconstructed mutual intensity that appears *less* coherent than the ground truth. Furthermore, noise also induces additional high frequency content in the reconstructed result. For the specific value of  $\alpha$  used, regularization using the nuclear norm only yields

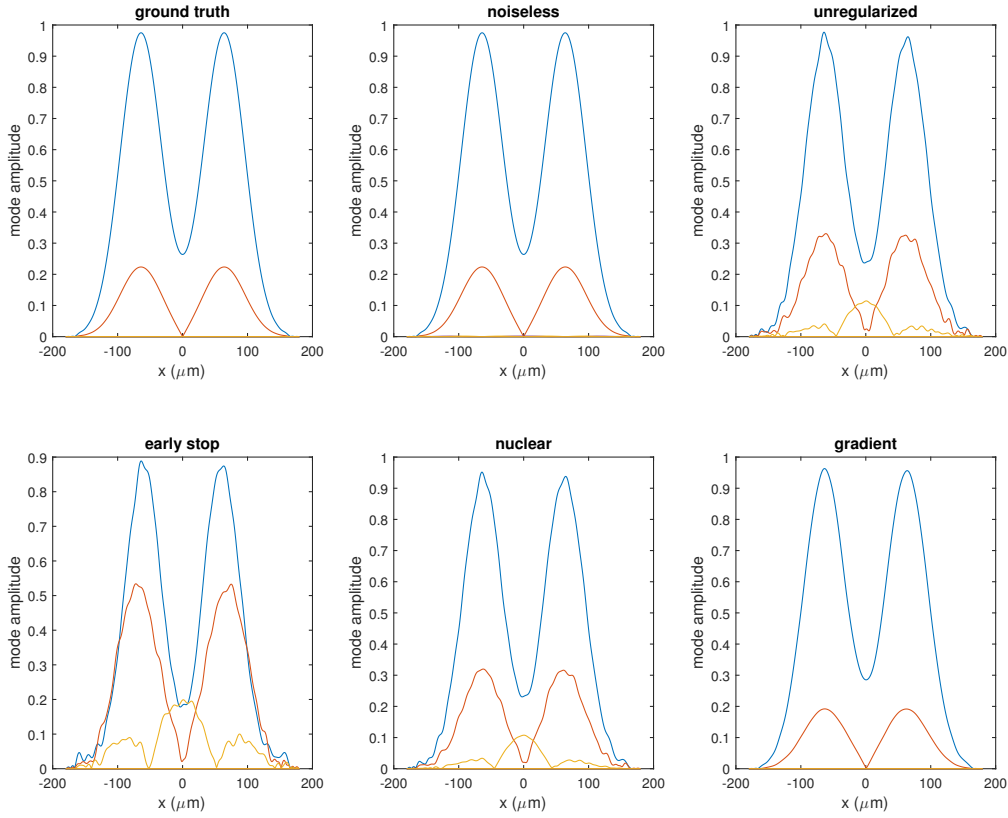


Figure 4. Amplitude plots of the 10 highest energy coherence modes for each mutual intensity function.

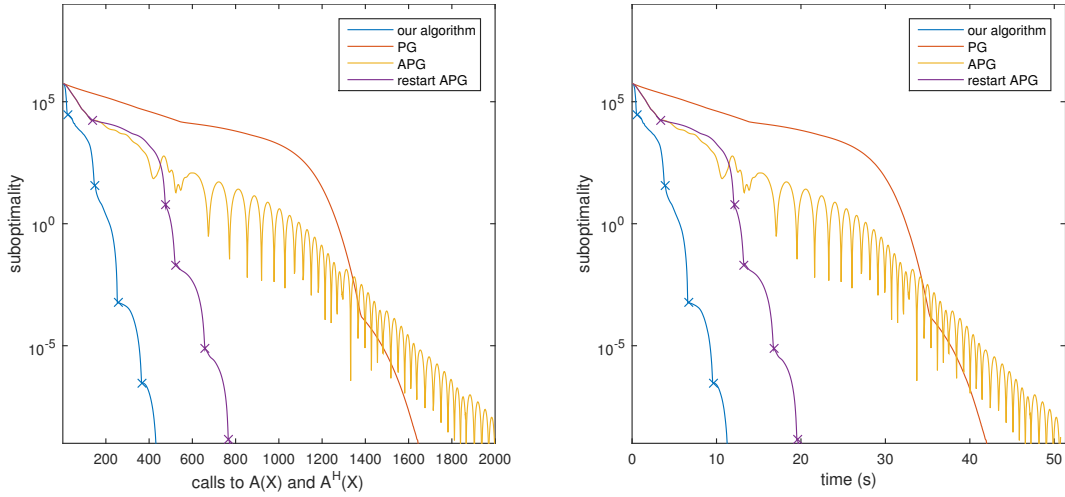


Figure 5. Comparison of convergence across different algorithms for the simulated data. The vertical axis is the difference between the value of  $f(\mathbf{X})$  and the lowest attained value of  $f(\mathbf{X})$  across all algorithms. On left, the horizontal axis is the number of invocations of the  $\mathcal{A}$  and  $\mathcal{A}^H$  operators, being the dominant part of computation time and invariant across platforms. On right, the horizontal axis is time taken. The  $\times$  mark where restarts occurred.

marginal improvements over the unregularized reconstruction, whereas regularization using the smoothness-inducing regularizer both smooths the result and reduces the number of significant modes back down to the correct number of modes. Of course, we can increase the  $\mu$  parameter for the nuclear norm case to reduce the number of modes, but it does not fully smooth the result and results in a mutual intensity that does not match the measurements as well as the smooth-prior regularized result. We note that the **early stop** result has the same amount of measurement mismatch as the two regularized solutions, showing how ill-posed the problem is and the necessity for regularization.

Our algorithm also converges faster than the three other methods given in Figure 5, albeit restart APG converges asymptotically as fast. Non-restarting APG oscillates due to excess critical momentum, as described in [25]. The advantages of our algorithm are that: (1) it is provably convergent, whereas to the best of our knowledge no proof of convergence has been given for the algorithm given in [25], and (2) it converges much faster than the provably convergent non-restarting APG (*i.e.*, FISTA [6]).

**5.2. Experimental Data.** We use the experimental data from [38], wherein the intensity profile of a partially coherent beam is imaged at 201 positions along the optical axis. The partially coherent beam was generated by focusing an LED light source through a 532 nm bandpass filter onto a 100  $\mu\text{m}$  slit located at the front focal plane of a 100 mm focal length cylindrical lens. A 500  $\mu\text{m}$  slit placed at the back focal plane is illuminated by light passing through the cylindrical lens, and this slit is imaged using a 50 mm cylindrical lens placed 150 mm after the slit. Based on visual inspection, the axial positions captured were located between  $z = -30.25$  mm and  $z = 19.75$  mm relative to the image of the slit.

The experimental data  $y_{ms}$  are taken from a single row on a camera with 3.2  $\mu\text{m}$  pitch, and the standard deviation  $\sigma_{ms}$  were estimated from the neighboring 16 rows. A visualization of the measured and theoretical intensities are shown in Figure 6. We use a sinc basis with sampling interval 6.4  $\mu\text{m}$  to discretize the mutual intensity into a  $101 \times 101$  matrix. We note that the field does not necessarily have a spatial band-limit compatible with the sampling interval, but since we only measure the intensity at intervals of 3.2  $\mu\text{m}$ , it would be very difficult to recover any information at a higher sampling rate and hence we ignore the higher frequency components. The smallest and largest singular values of the matrix  $\mathbf{A}$  as it is defined in subsection 4.2 were  $a_{\min} = 4.263$  and  $a_{\max} = 7.925$ .

While ground truth is not available, an aberration-free theoretical estimate of the mutual intensity is:

$$(21) \quad J(x_1, x_2) \propto \text{rect}(\beta_1 x_1) \text{rect}(\beta_1 x_2) \text{sinc}(\beta_2(x_1 - x_2)) \exp(i\beta_3(x_1^2 - x_2^2)) \otimes \text{sinc}(x_1/\Delta) \text{sinc}(x_2/\Delta)$$

where  $\beta_1 = 4 \text{ mm}^{-1}$ ,  $\beta_2^{-1} = 532 \mu\text{m}$ ,  $\beta_3 = 1.9684 \times 10^{-4} \mu\text{m}^{-2}$  and  $\Delta = 6.4 \mu\text{m}$  is the sampling interval. We use this aberration-free estimate only as a rough point of reference; it is not intended to be interpreted as the ground truth.

We again use several different sets of parameters for our algorithm; the only difference from the simulated data is the addition of another regularizer and a different value of  $\alpha$  for the target value of  $\frac{1}{2} \|\mathcal{A}(\mathbf{X}) - \mathbf{b}\|_2^2$  in the **early stop** and regularized reconstructions. We introduce a new input data set window whose matrix  $\mathbf{D}$  is a diagonal matrix; the elements corresponding to the center 250  $\mu\text{m}$  region are unity and the other elements rise linearly away

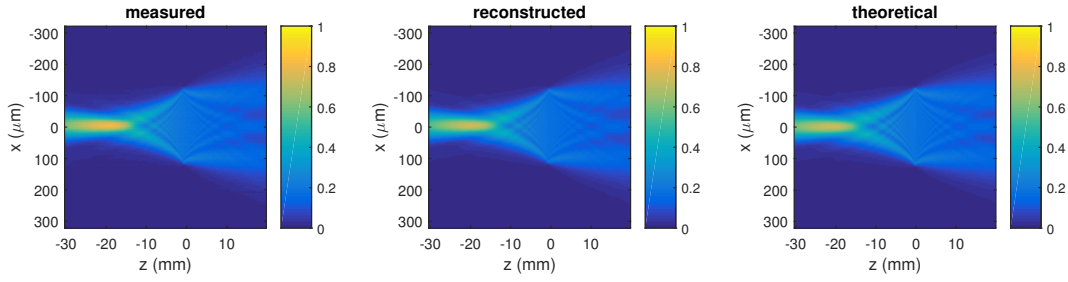


**Figure 6.** Noisy measurements of the intensity are shown on left, with the theoretical aberration-free intensity profile shown on the right. Propagated intensity of a regularized reconstructed result is shown in center. In all images, light propagates from left to right, and the intensity is in arbitrary units. The theoretical intensity is provided as a point of reference and is not necessarily the ground truth.

from this region, up to a maximum of 391 at the ends. The idea is that since we know our slit should be imaged to a region that wide, we would like to penalize any contributions outside of this region. However, we do not want to assume the field outside to be zero, due to the presence of possible aberrations in the system. Hence, this regularizer is a gentler way of finding a less energetic solution while at the same time preferring to remove energy from areas where we do not expect much energy to be present. Coincidentally, this regularizer is also equivalent to imposing some sort of smoothness constraint on the intensity in the far field of the partially coherent beam. We also chose a value of  $\alpha = 5$  to account for additional possible error in  $\mathcal{A}$  (due to imperfect equipment and calibration) and standard deviation estimation.

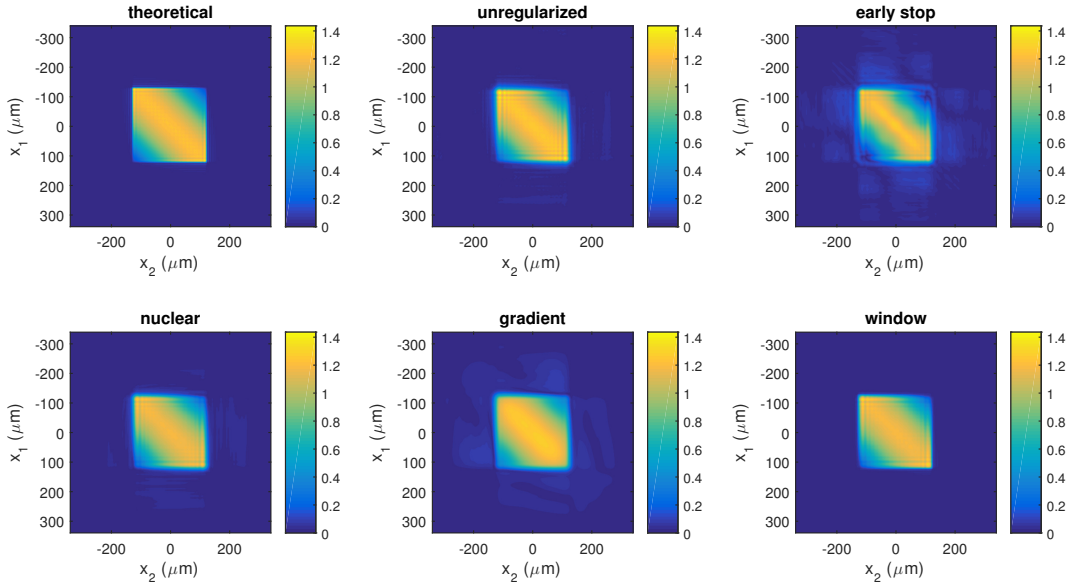


**Figure 7.** Magnitude of the mutual intensity functions for the experimental data. They are all drawn using the same scale, normalized to the maximum magnitude of the theoretical result.

The reconstructed mutual intensity functions are shown in Figure 7 with modes shown in

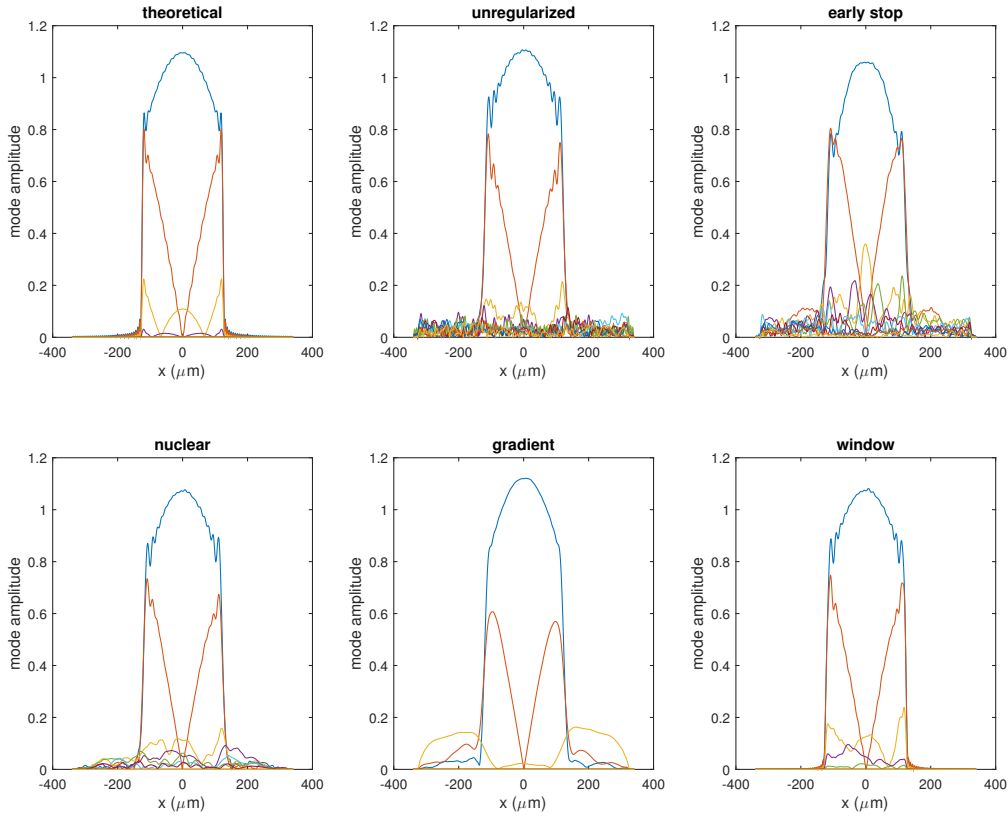


Figure 8. Amplitude plots of the 10 highest energy coherence modes for each mutual intensity function.

	unregularized	early stop	nuclear	gradient	window
normalized RMSE	0.2363	0.3649	0.2317	0.2189	0.2176
trace distance	0.1795	0.2785	0.1666	0.1743	0.1486

Table 2

Quantitative measurements of the difference between the mutual intensity matrices reconstructed from experimental data and the aberration-free mutual intensity estimate. The quantities are defined in the same way as Table 1, with the aberration-free mutual intensity estimate taken as the “truth”.

Figure 8. We give quantitative comparisons between the theoretical mutual intensity and the reconstructed mutual intensity in Table 2, and a comparison of algorithm convergence is given in Figure 9. All regularized solutions remove some amount of noise, as evident in the increased smoothness and reduction of high order mode energy in the coherence modes visualization. The **nuclear** result cleans up the reconstruction compared to the noisy reconstruction, but it still leaves a lot of excess energy in the higher order modes, especially energy outside the region occupied by the slit. The **gradient** regularizer is the best at reducing the number of modes, but it oversmooths the result—the third mode (light orange as seen in Figure 8) spills outside of the region occupied by the slit and resembles neither the third mode from the theoretical results nor that of the noisy results, and the sharp edges of the second mode

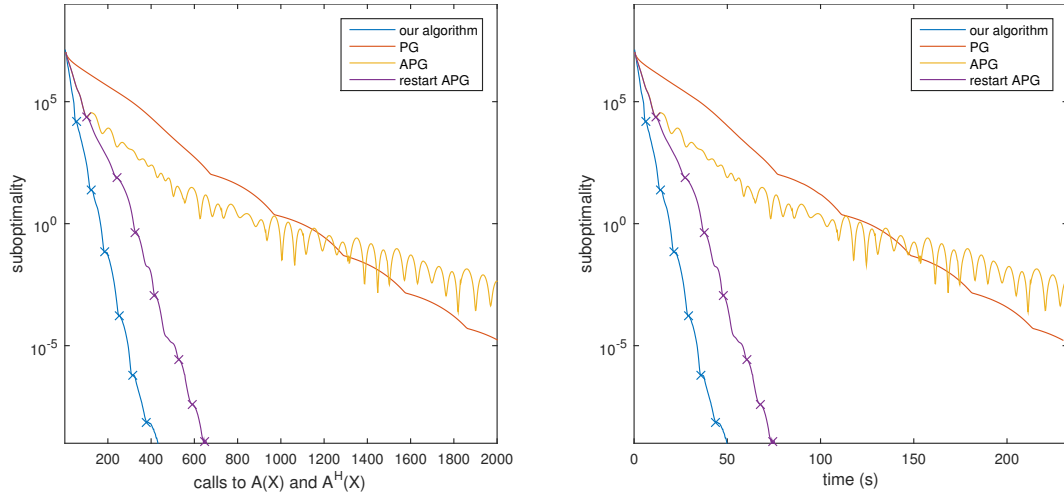


**Figure 9.** Comparison of convergence across different algorithms for the experimental data. The vertical axis is the difference between the value of  $f(\mathbf{X})$  and the lowest attained value of  $f(\mathbf{X})$  across all algorithms. On left, the horizontal axis is the number of invocations of the  $\mathcal{A}$  and  $\mathcal{A}^H$  operators, being the dominant part of computation time and invariant across platforms. On right, the horizontal axis is time taken. The  $\times$ s mark where restarts occurred.

(dark orange) are gone. The image of the magnitude of the mutual intensity in Figure 7 is also quite blurry.

While the `nuclear` result is an improvement over the unregularized result, it is obvious that applying additional prior information in the design for `window`'s regularizer yields a much better reconstruction. The first three mode profiles are reconstructed fairly well, as can be seen in Figure 8, and there is only slightly more energy in the higher order modes. The spatial extent of the reconstruction is also much more confined compared to the other reconstructions.

The experimental data convergence results in Figure 9 are quite similar to the one for the simulated data—our algorithm has an asymptotic convergence rate comparable to gradient restart APG, albeit we again reach the fast convergence regime faster.

**6. Conclusion.** We have demonstrated that trace-regularized coherence retrieval can be a powerful tool in recovering the mutual intensity when the inverse problem is ill-conditioned. The generalization of the nuclear-norm enables flexibility in applying *a priori* information, leading to higher quality reconstructions. Furthermore, we have demonstrated an efficient numerical scheme for our coherence retrieval model, with performance at worst comparable to the state-of-the-art adaptive restart APG scheme while simultaneously being provably globally convergent, with mild conditions required for linear convergence.

This work leverages very simple  $\mathbf{D}$  matrices for regularization with good results, but more flexibility and power can be attained from leveraging the framework of tight frames through further study. Furthermore, a method for exploiting redundant information in the measurements to calibrate real-world  $\mathbf{K}_m$ s as well as methods to reduce the memory and computational footprint for high dimensional structured mutual intensity matrices are all potential avenues for future exploration.

## REFERENCES

- [1] T. ASAKURA, H. FUJII, AND K. MURATA, *Measurement of spatial coherence using speckle patterns*, *Optica Acta: Int. J. Opt.*, 19 (1972), pp. 273–290.
- [2] H. ATTOUCH, J. BOLTE, P. REDONT, AND A. SOUBEYRAN, *Proximal alternating minimization and projection methods for nonconvex problems: An approach based on the Kurdyka-Lojasiewicz inequality*, *Math. Oper. Res.*, 35 (2010), pp. 438–457.
- [3] J. C. BARREIRO AND J. OJEDA-CASTAÑEDA, *Degree of coherence: a lensless measuring technique*, *Opt. Lett.*, 18 (1993), pp. 302–304.
- [4] H. O. BARTELT, K.-H. BRENNER, AND A. W. LOHMANN, *The Wigner distribution function and its optical production*, *Opt. Commun.*, 32 (1980), pp. 32–38.
- [5] J. BARZILAI AND J. M. BORWEIN, *Two-point step size gradient methods*, *IAM J. Numer. Anal.*, 8 (1988), pp. 141–148.
- [6] A. BECK AND M. TEBoulLE, *A fast iterative shrinkage-thresholding algorithm for linear inverse problems*, *SIAM J. Imaging Sci.*, 2 (2009), pp. 183–202.
- [7] J. BOLTE, S. SABACH, AND M. TEBoulLE, *Proximal alternating linearized minimization for nonconvex and nonsmooth problems*, *Math. Prog.*, 146 (2014), pp. 459–494.
- [8] M. BORN AND E. WOLF, *Principles of Optics, 7th. ed.*, Cambridge University Press, Cambridge, UK, 2005.
- [9] G. J. BURTON AND I. R. MOORHEAD, *Color and spatial structure in natural scenes*, *Appl. Opt.*, 26 (1987), pp. 157–170.
- [10] J.-F. CAI, B. DONG, S. OSHER, AND Z. SHEN, *Image restoration: total variation, wavelet frames, and beyond*, *J. Am. Math. Soc.*, 25 (2012), pp. 1033–1089.
- [11] J. N. CLARK, X. HUANG, R. J. HARDER, AND I. K. ROBINSON, *Dynamic imaging using ptychography*, *Phys. Rev. Lett.*, 112 (2014), p. 113901.
- [12] Y. CUI, D. SUN, AND K.-C. TOH, *On the asymptotic superlinear convergence of the augmented lagrangian method for semidefinite programming with multiple solutions*, arXiv preprint arXiv:1610.00875, (2016).
- [13] B. DONG AND Z. SHEN, *MRA-based wavelet frames and applications*, IAS/Park city mathematics series: the mathematics of image processing, 19 (2010), pp. 7–158.
- [14] D. DRAGOMAN, *Unambiguous coherence retrieval from intensity measurements*, *J. Opt. Soc. Am. A*, 20 (2003), pp. 290–295.
- [15] D. J. FIELD, *Relations between the statistics of natural images and the response properties of cortical cells*, *J. Opt. Soc. Am. A*, 4 (1987), pp. 2379–2394.
- [16] J. W. GOODMAN, *Statistical Optics*, Wiley Interscience, New York, 1985.
- [17] M. LEVOY, Z. ZHANG, AND I. MCDOWALL, *Recording and controlling the 4D light field in a microscope*, *J. Microsc.*, 235 (2009), pp. 144–162.
- [18] Y. LI, G. EICHMANN, AND M. CONNER, *Optical Wigner distribution and ambiguity function for complex signals and images*, *Opt. Commun.*, 67 (1988), pp. 177–179.
- [19] D. M. MARKS, R. A. STACK, AND D. J. BRADY, *Astigmatic coherence sensor for digital imaging*, *Opt. Lett.*, 25 (2000), pp. 1726–1728.
- [20] D. F. MCALISTER, M. BECK, L. CLARKE, A. MAYER, AND M. G. RAYMER, *Optical phase retrieval by phase-space tomography and fractional-order Fourier transforms*, *Opt. Lett.*, 20 (1995), pp. 1181–1183.
- [21] M. MICHALSKI, E. E. SICRE, AND H. J. RABAL, *Display of the complex degree of coherence due to quasi-monochromatic spatially incoherent sources*, *Opt. Lett.*, 10 (1985), pp. 585–587.
- [22] Y. NESTEROV, *Introductory lectures on convex optimization: A basic course*, vol. 87, Springer Science & Business Media, 2013.
- [23] R. NG, *Fourier slice photography*, in Proc. ACM SIGGRAPH, 2005.
- [24] R. NG, M. LEVOY, M. BRÉDIF, G. DUVAL, M. HOROWITZ, AND P. HANRAHAN, *Light field photography with a hand-held plenoptic camera*, Tech. Report CTSR 2005-02, Stanford University, 2005.
- [25] B. O’DONOGHUE AND E. CANDÈS, *Adaptive restart for accelerated gradient schemes*, *Found. Comp. Math.*, 15 (2015), pp. 715–732.
- [26] M. G. RAYMER, M. BECK, AND D. MCALISTER, *Complex wave-field reconstruction using phase-space tomography*, *Phys. Rev. Lett.*, 72 (1994), pp. 1137–1140.

- [27] C. RYDBERG AND J. BENGTSSON, *Numerical algorithm for the retrieval of spatial coherence properties of partially coherent beams from transverse intensity measurements*, Opt. Express, 15 (2007), pp. 13613–13623.
- [28] A. STARIKOV AND E. WOLF, *Coherent-mode representation of Gaussian Schell-model sources and of their radiation fields*, J. Opt. Soc. Am., 72 (1982), pp. 923–928.
- [29] B. STOKLASA, L. MOTKA, J. REHACEK, Z. HRADIL, AND L. SÁNCHEZ-SOTO, *Wavefront sensing reveals optical coherence*, Nat. Commun., 5 (2014).
- [30] W. SU, S. BOYD, AND E. CANDÈS, *A differential equation for modeling Nesterov’s accelerated gradient method: Theory and insights*, in NIPS, 2014, pp. 2510–2518.
- [31] M. TESTORF, B. HENNELLY, AND J. OJEDA-CASTAÑEDA, *Phase-Space Optics: Fundamentals and Applications*, McGraw-Hill Education, 2009.
- [32] B. J. THOMPSON AND E. WOLF, *Two-beam interference with partially coherent light*, J. Opt. Soc. Am., 47 (1957), p. 895.
- [33] L. TIAN, J. LEE, S. B. OH, AND G. BARBASTATHIS, *Experimental compressive phase space tomography*, Opt. Express, 20 (2012), pp. 8296–8308.
- [34] L. TIAN, Z. ZHANG, J. C. PETRUCCELLI, AND G. BARBASTATHIS, *Wigner function measurement using a lenslet array*, Opt. Express, 21 (2013), pp. 10511–10525.
- [35] D. J. TOLHURST, Y. TADMOR, AND T. CHAO, *Amplitude spectra of natural images*, Ophthalmic and Physiological Optics, 12 (1992), pp. 229–232.
- [36] L. WALLER, G. SITU, AND J. W. FLEISCHER, *Phase-space measurement and coherence synthesis of optical beams*, Nat. Photon., 6 (2012), pp. 474–479.
- [37] E. WOLF, *New theory of partial coherence in the space-frequency domain. Part I: spectra and cross spectra of steady-state sources*, J. Opt. Soc. Am., 72 (1982), pp. 343–351.
- [38] Z. ZHANG, Z. CHEN, S. REHMAN, AND G. BARBASTATHIS, *Factored form descent: a practical algorithm for coherence retrieval*, Opt. Express, 21 (2013), pp. 5759–5780.
- [39] Z. ZHANG AND M. LEVOY, *Wigner distributions and how they relate to the light field*, in ICCP, 2009, pp. 1–10.

**Appendix A. Proof of Theorem 4.2.** Given  $\eta \in (0, +\infty]$ , define  $\Phi_\eta$  be the class of all concave and continuous functions  $\phi : [0, \eta] \rightarrow \mathbb{R}_+$  that satisfy  $\phi(0) = 0$ ,  $\phi$  is  $C^1$  on  $(0, \eta)$  and continuous at 0, and  $\phi'(s) > 0, \forall s \in (0, \eta)$ .

**Definition A.1.** Let  $f : \mathbb{R}^n \rightarrow (-\infty, +\infty]$  be proper and lower semicontinuous. The function  $f$  is said to satisfy the Kurdyka-Łojasiewicz (KL) inequality at  $\bar{\mathbf{x}} \in \text{dom}(\partial f)$  if there exist  $\eta \in (0, +\infty]$ , a neighborhood  $\mathcal{U}$  of  $\bar{\mathbf{x}}$  and a function  $\phi \in \Phi_\eta$ , such that for all  $\mathbf{x} \in \mathcal{U} \cap [f(\bar{\mathbf{x}}) < f(\mathbf{x}) < f(\bar{\mathbf{x}}) + \eta]$ , the following inequality holds:

$$(22) \quad \phi'(f(\mathbf{x}) - f(\bar{\mathbf{x}})) \text{dist}(\mathbf{0}, \partial f(\mathbf{x})) \geq 1.$$

A function  $f(\mathbf{x})$  is called a KL function if  $f$  satisfies the KL property at every  $\mathbf{x} \in \text{dom}(\partial f)$ . We will now show some basic properties of Algorithm 1 in the following lemmas and use them to prove the global convergence of Algorithm 1.

**Lemma A.1.** Let  $\{\mathbf{X}_k\}$  be the sequence generated by Algorithm 1. Then, there exists  $a, b > 0$  and  $\bar{w} \in [0, 1)$  such that for all  $k \geq 0$ , we have

$$(23) \quad h(\mathbf{X}_k) - h(\mathbf{X}_{k+1}) \geq a \|\mathbf{X}_k - \mathbf{X}_{k+1}\|_{\mathbb{F}}^2,$$

$$(24) \quad \text{dist}(\mathbf{0}, \partial h(\mathbf{X}_{k+1})) \leq b(\|\mathbf{X}_{k+1} - \mathbf{X}_k\|_{\mathbb{F}} + \bar{w} \|\mathbf{X}_k - \mathbf{X}_{k-1}\|_{\mathbb{F}}).$$

*Proof.* Define

$$(25) \quad \mathbf{W}_{k+1} = \text{Prox}_g^{\alpha_k}(\mathbf{X}_k - \alpha_k \nabla f(\mathbf{X}_k)).$$

Let  $\Omega_1 = \{k : \mathbf{X}_{k+1} = \mathbf{W}_{k+1}, k > 1\}$  and  $\Omega_2 = \{k : \mathbf{X}_{k+1} = \mathbf{Z}_{k+1}\}$  where  $\mathbf{Z}_{k+1}$  is defined in (13). Then,  $\Omega_1 \cap \Omega_2 = \emptyset$  and  $\Omega_1 \cup \Omega_2 = \mathbb{N}$ . We consider two cases: (I)  $k \in \Omega_1$  and (II)  $k \in \Omega_2$ . **Case I.**  $k \in \Omega_1$  implies that  $\mathbf{X}_k = \mathbf{Y}_k$ , and hence  $h(\mathbf{X}_k) - h(\mathbf{X}_{k+1}) \geq \delta \|\mathbf{X}_k - \mathbf{X}_{k+1}\|_{\mathbb{F}}^2$  due to inequality (15) from the step size estimation process. From the optimality condition of (25), we know

$$(26) \quad \frac{1}{\alpha_k}(\mathbf{X}_k - \mathbf{X}_{k+1}) - \nabla f(\mathbf{X}_k) \in \partial g(\mathbf{X}_{k+1}).$$

The inequality (26) implies

$$\begin{aligned} \text{dist}(0, \partial h(\mathbf{X}_{k+1})) &\leq \left\| \nabla f(\mathbf{X}_{k+1}) + \frac{1}{\alpha_k}(\mathbf{X}_k - \mathbf{X}_{k+1}) - \nabla f(\mathbf{X}_k) \right\|_{\mathbb{F}} \\ &\leq (L + 1/\alpha_{\min}) \|\mathbf{X}_{k+1} - \mathbf{X}_k\|_{\mathbb{F}}. \end{aligned}$$

since  $\alpha_k \geq \alpha_{\min} > 0, \forall k$ .

**Case II:**  $k \in \Omega_2$ . From the first order optimality condition of (13), we have

$$(27) \quad \frac{1}{\alpha_k}(\mathbf{Y}_k - \mathbf{Z}_{k+1}) - \nabla f(\mathbf{Y}_k) \in \partial g(\mathbf{Z}_{k+1}).$$

Then, together with the convexity of  $h$  and the fact that  $\mathbf{X}_{k+1} = \mathbf{Z}_{k+1}$ , we have

$$\begin{aligned} h(\mathbf{X}_k) - h(\mathbf{X}_{k+1}) &\geq \left\langle \nabla f(\mathbf{Z}_{k+1}) + \frac{1}{\alpha_k}(\mathbf{Y}_k - \mathbf{Z}_{k+1}) - \nabla f(\mathbf{Y}_k), \mathbf{X}_k - \mathbf{Z}_{k+1} \right\rangle \\ &= \left\langle \left( \frac{1}{\alpha_k} \mathbf{I} - \mathcal{A}_* \mathcal{A} \right) (\mathbf{Y}_k - \mathbf{Z}_{k+1}), \mathbf{X}_k - \mathbf{Z}_{k+1} \right\rangle \\ &\geq \frac{\gamma}{\alpha_{\max}} \|\mathbf{X}_k - \mathbf{X}_{k+1}\|_{\mathbb{F}}^2, \end{aligned}$$

since the inequality (14) holds and  $0 < \alpha_{\min} \leq \alpha_k \leq \alpha_{\max}$ . Moreover, the inequality

$$\begin{aligned} \text{dist}(0, \partial h(\mathbf{X}_{k+1})) &\leq \left\| \nabla f(\mathbf{Z}_{k+1}) + \frac{1}{\alpha_k}(\mathbf{Y}_k - \mathbf{Z}_{k+1}) - \nabla f(\mathbf{Y}_k) \right\|_{\mathbb{F}} \\ &\leq (L + 1/\alpha_{\min})(\|\mathbf{X}_{k+1} - \mathbf{X}_k\|_{\mathbb{F}} + \bar{w} \|\mathbf{X}_k - \mathbf{X}_{k-1}\|_{\mathbb{F}}) \end{aligned}$$

holds where  $\bar{w} \in [0, 1)$  since  $(t_k - 1)/t_{k+1} < 1$  for all  $k \leq k_{\text{resmax}}$ .

Consequently, the two cases yield that the inequality (23) holds with  $a = \min(\delta, \gamma/\alpha_{\max}) > 0$  and the inequality (24) holds with  $b = L + 1/\alpha_{\min} > 0$ .  $\blacksquare$

Denote  $w(\mathbf{X}_0)$  to be the limiting points of  $\{\mathbf{X}_k\}$ . The next lemma shows that Algorithm 1 is subsequence convergent, *i.e.*, all the convergent subsequences converge to a minimal point when the generated sequence is bounded.

**Lemma A.2.** *Let  $\{\mathbf{X}_k\}$  be the sequence generated by Algorithm 1 starting from  $\mathbf{X}_0$ . If  $\{\mathbf{X}_k\}$  is bounded, then  $w(\mathbf{X}_0)$  is a non-empty compact set, and  $w(\mathbf{X}_0) \subseteq \mathcal{X}_* \neq \emptyset$ .*

*Proof.* Since the sequence  $\{\mathbf{X}_k\}$  is bounded,  $w(\mathbf{X}_0)$  is non-empty. Meanwhile,  $w(\mathbf{X}_0)$  is compact since it is the intersection of compact sets, *i.e.*,  $w(\mathbf{X}_0) = \bigcap_{q \in \mathbb{N}} \overline{\bigcup_{k \geq q} \{\mathbf{X}_k\}}$ , where  $\overline{\mathcal{A}}$  denotes the closure of set  $\mathcal{A}$ . Let  $\bar{\mathbf{X}}$  be any point in  $w(\mathbf{X}_0)$  and  $\{\mathbf{X}_{k_j}\}$  be a convergent subsequence of  $\{\mathbf{X}_k\}$  such that  $\mathbf{X}_{k_j} \rightarrow \bar{\mathbf{X}}$  as  $j \rightarrow +\infty$ . Since  $\mathbf{D} \in \mathcal{S}_+^N$ ,  $h(\mathbf{X}) \geq 0, \forall \mathbf{X}$ .

Together with the inequality (23), we know there exists some  $\bar{h}$  such that  $h(\mathbf{X}_k) \rightarrow \bar{h}$  as  $k \rightarrow +\infty$ . Moreover, (23) implies

$$a \sum_{k=0}^{\infty} \|\mathbf{X}_k - \mathbf{X}_{k+1}\|_{\mathbb{F}}^2 \leq \sum_{k=0}^{\infty} (h(\mathbf{X}_k) - h(\mathbf{X}_{k+1})) \leq h(\mathbf{X}_0) - \bar{h} < +\infty.$$

So, we have  $\|\mathbf{X}_{k_j+1} - \mathbf{X}_{k_j}\|_{\mathbb{F}} \rightarrow 0$  and  $\|\mathbf{X}_{k_j} - \mathbf{X}_{k_j-1}\|_{\mathbb{F}} \rightarrow 0$  as  $k \rightarrow +\infty$ . Moreover, from the above facts, it is easy to prove that  $\{\mathbf{X}_{k_j+1}\}$  also converges to  $\bar{\mathbf{X}}$ . Together with (24), we know  $\text{dist}(\mathbf{0}, \partial h(\mathbf{X}_{k_j+1})) \rightarrow 0$  as  $j \rightarrow +\infty$ . Let  $\mathcal{U}$  be a neighborhood of  $\bar{\mathbf{X}}$  with radius  $M$ . Then, we have

$$(28) \quad h(\mathbf{X}) \geq h(\mathbf{X}_{k_j+1}) - \text{dist}(\mathbf{0}, \partial h(\mathbf{X}_{k_j+1})) \|\mathbf{X} - \mathbf{X}_{k_j+1}\|_{\mathbb{F}}, \quad \forall \mathbf{X} \in \mathcal{U}.$$

Since  $\lim_{j \rightarrow +\infty} h(\mathbf{X}_{k_j+1}) = h(\bar{\mathbf{X}})$ , taking the limit  $j \rightarrow +\infty$  in (28), we have  $h(\mathbf{X}) \geq h(\bar{\mathbf{X}})$  for all  $\mathbf{X} \in \mathcal{U}$ . By the convexity of  $h$ ,  $\bar{\mathbf{X}}$  is a global minima of (8), i.e.  $\mathbf{0} \in \partial h(\bar{\mathbf{X}})$ .  $\blacksquare$

Based on the proof of Theorem 1 in [7], we can prove the theorem 4.2 as follows.

*Proof.* It is noted that the objective function  $h$  in (8) is a KL function as both  $f$  and  $g$  are semi-algebraic. Since  $\{\mathbf{X}_k\}$  is bounded,  $w(\mathbf{X}_0)$  is not empty. Denote  $h(\mathbf{X}) = \bar{h}$  for all  $\mathbf{X} \in w(\mathbf{X}_0)$  as  $\mathbf{0} \in \partial h(\mathbf{X}), \forall \mathbf{X} \in w(\mathbf{X}_0)$  from Lemma A.2. Let  $\{\mathbf{X}_{k_j}\}$  be a convergent subsequence of  $\{\mathbf{X}_k\}$  such that  $\mathbf{X}_{k_j} \rightarrow \bar{\mathbf{X}}$  as  $j \rightarrow +\infty$ . Since  $\mathbf{X}_k \in \mathcal{S}_+^N, \forall k$  the decreasing property (23) yields  $\lim_{k \rightarrow +\infty} h(\mathbf{X}_k) = \lim_{j \rightarrow +\infty} h(\mathbf{X}_{k_j}) = \bar{h}$ . Moreover, we assume that  $h(\mathbf{X}_k) > \bar{h}$  for all  $k$ . Otherwise, if there exists some  $k_0$  such that  $h(\mathbf{X}_{k_0}) = \bar{h}$ , from the decreasing property (23) and  $h(\mathbf{X}_k) \geq \bar{h}$ , we know  $\mathbf{X}_k = \mathbf{X}_{k_0}$  for all  $k \geq k_0$ . By the definition of  $w(\mathbf{X}_0)$ , we have  $\lim_{k \rightarrow +\infty} \text{dist}(\mathbf{X}_k, w(\mathbf{X}_0)) = 0$ . Applying the uniformized KL property ([7], Lemma 6) of  $h$  on  $w(\mathbf{X}_0)$ , there exist  $k_\ell > 0, \eta > 0$  and  $\phi \in \Phi_\eta$  such that for all  $\bar{\mathbf{X}} \in w(\mathbf{X}_0)$ , we have

$$(29) \quad \phi'(h(\mathbf{X}_k) - \bar{h}) \text{dist}(\mathbf{0}, \partial h(\mathbf{X}_k)) \geq 1, \quad \forall k > k_\ell.$$

By the inequality (24), (29) implies

$$(30) \quad \phi'(h(\mathbf{X}_k) - \bar{h}) \geq \frac{1}{b(\|\mathbf{X}_k - \mathbf{X}_{k-1}\|_{\mathbb{F}} + \bar{w}\|\mathbf{X}_{k-1} - \mathbf{X}_{k-2}\|_{\mathbb{F}})}, \quad \forall k > k_\ell.$$

By the concavity of  $\phi$  (23) and (30), we know that

$$(31) \quad \begin{aligned} \Delta_{k,k+1} &:= \phi(h(\mathbf{X}_k) - \bar{h}) - \phi(h(\mathbf{X}_{k+1}) - \bar{h}) \\ &\geq \phi'(h(\mathbf{X}_k) - \bar{h})(h(\mathbf{X}_k) - h(\mathbf{X}_{k+1})) \geq \frac{a\|\mathbf{X}_{k+1} - \mathbf{X}_k\|_{\mathbb{F}}^2}{b(\|\mathbf{X}_k - \mathbf{X}_{k-1}\|_{\mathbb{F}} + \bar{w}\|\mathbf{X}_{k-1} - \mathbf{X}_{k-2}\|_{\mathbb{F}})} \end{aligned}$$

Define  $C = b/a > 0$  in (31) and from the geometric inequality, we have

$$(32) \quad 2\|\mathbf{X}_k - \mathbf{X}_{k+1}\|_{\mathbb{F}} \leq \|\mathbf{X}_k - \mathbf{X}_{k-1}\|_{\mathbb{F}} + \bar{w}\|\mathbf{X}_{k-1} - \mathbf{X}_{k-2}\|_{\mathbb{F}} + C\Delta_{k,k+1}$$

For any  $k > k_\ell$ , summing up (32) from  $i = k_\ell + 1, \dots, k$ , we have

$$(33) \quad \begin{aligned} 2 \sum_{i=k_\ell+1}^k \|\mathbf{X}_i - \mathbf{X}_{i+1}\|_F &\leq \sum_{i=k_\ell+1}^k \|\mathbf{X}_i - \mathbf{X}_{i-1}\|_F + \bar{w} \|\mathbf{X}_{i-1} - \mathbf{X}_{i-2}\|_F + C\Delta_{i,i+1} \\ &\leq (1 + \bar{w}) \sum_{i=k_\ell-1}^k \|\mathbf{X}_{i+1} - \mathbf{X}_i\|_F + C\Delta_{k_\ell+1,k+1} \end{aligned}$$

where the last inequality is from the fact that  $\Delta_{p,q} + \Delta_{q,r} = \Delta_{p,r}$  for all  $p, q, r \in \mathbb{N}$ . Since  $\phi \geq 0$  and  $\bar{w} \in [0, 1)$ , the inequality (33) implies

$$(34) \quad (1 - \bar{w}) \sum_{i=k_\ell+1}^k \|\mathbf{X}_i - \mathbf{X}_{i+1}\|_F \leq (1 + \bar{w}) \sum_{i=k_\ell-1}^{k_\ell} \|\mathbf{X}_{i+1} - \mathbf{X}_i\|_F + C\phi(h(\mathbf{X}_{k_\ell}) - \bar{h})$$

Let  $k \rightarrow +\infty$  in (34), we know  $\sum_{k=1}^{+\infty} \|\mathbf{X}_k - \mathbf{X}_{k-1}\|_F < +\infty$  which implies that  $\{\mathbf{X}_k\}$  is converges to a  $\bar{\mathbf{X}} = w(\mathbf{X}_0)$  and so  $0 \in \partial h(\bar{\mathbf{X}})$ .  $\blacksquare$

**Appendix B. Proof of Proposition 4.1.** By the decreasing property (23), it is sufficient to show that the sub-level set  $[h(\mathbf{X}) \leq h_0]$  is bounded where  $h_0 = h(\mathbf{X}_0)$ . Given any  $\mathbf{X} \in [h(\mathbf{X}) \leq h_0]$ , we have  $\mathbf{X} \in \mathcal{S}_+^N$  and  $f(\mathbf{X}) \leq h_0$ . Then, there exists some  $\mathbf{Y} \in \mathbb{C}^{N \times N}$  such that  $\mathbf{X} = \mathbf{Y}\mathbf{Y}^H$  with

$$(35) \quad \frac{1}{2} \left\| \mathcal{A}(\mathbf{Y}\mathbf{Y}^H) - \mathbf{b} \right\|_2^2 + \mu \langle \mathbf{D}, \mathbf{Y}\mathbf{Y}^H \rangle \leq h_0.$$

By the triangle inequality, (35) implies

$$\left\| \mathcal{A}(\mathbf{Y}\mathbf{Y}^H) \right\|_2 \leq \sqrt{2h_0} + \|\mathbf{b}\|_2.$$

as  $\mathbf{D} \in \mathcal{S}_+^N$  and  $\mu \geq 0$ . Standard norm inequalities gives:

$$\left\| \mathcal{A}(\mathbf{Y}\mathbf{Y}^H) \right\|_1 \leq \sqrt{M} \left( \sqrt{2h_0} + \|\mathbf{b}\|_2 \right).$$

We note here that we can also write

$$\mathcal{A}(\mathbf{Y}\mathbf{Y}^H) = \mathbf{C} \left[ (\mathbf{A}\mathbf{Y}) \odot (\mathbf{A}\mathbf{Y})^* \right] \mathbf{1}$$

where  $\odot$  denotes the element-wise (Hadamard) product,  $\mathbf{1} \in \mathbb{R}^N$  of all 1s, and  $\mathbf{C} \in \mathbb{R}^{M \times MN}$  is a blockwise diagonal matrix whose  $m$ th block is equal to  $\mathbf{1}^\top / \sigma_m$ . Let  $\sigma_{\max}$  denote the minimal value among the  $\sigma_m$ s. Since the bracketed expression is the element-wise magnitude squared of  $\mathbf{A}\mathbf{Y}$  and hence nonnegative, we then have

$$\|\mathbf{A}\mathbf{Y}\|_F^2 \leq \sigma_{\max} \sqrt{M} \left( \sqrt{2h_0} + \|\mathbf{b}\|_2 \right).$$

Since  $\mathbf{A}$  has full column rank, we obtain that

$$\|\mathbf{Y}\|_F^2 \leq \frac{\sigma_{\max} \sqrt{M}}{a_{\min}^2} \left( \sqrt{2h_0} + \|\mathbf{b}\|_2 \right),$$

where  $a_{\min} > 0$  the smallest nonzero singular value of  $\mathbf{A}$ . Since  $\mathbf{X} = \mathbf{Y}\mathbf{Y}^H$ , the above inequality implies that the nuclear norm of  $\mathbf{X}$  is bounded:

$$\|\mathbf{X}\|_* \leq \frac{\sigma_{\max}\sqrt{M}}{a_{\min}^2} \left( \sqrt{2h_0} + \|\mathbf{b}\|_2 \right)$$

and hence  $\mathbf{X}$  must be bounded assuming bounded  $\mathbf{b}$  and finite  $\sigma_{\max}$ , and hence the sub-level set must also be bounded.

**Appendix C. Proof of Proposition 4.2.** The dual problem of (8) is

$$(36) \quad \min_{\mathbf{w}, \mathbf{S}} \frac{1}{2} \|\mathbf{w} - \mathbf{b}\|_2^2 + \iota_{\mathcal{S}_+^N}(\mathbf{S}), \text{ s.t. } \mathcal{A}^H(\mathbf{w}) + \mathbf{S} = \mathbf{D}.$$

The Lagrangian function  $\ell$  associated with the problem (36) is

$$\ell(\mathbf{w}, \mathbf{S}; \mathbf{X}) = \frac{1}{2} \|\mathbf{w} - \mathbf{b}\|_2^2 + \iota_{\mathcal{S}_+^N}(\mathbf{S}) + \langle \mathbf{X}, \mathcal{A}^H(\mathbf{w}) + \mathbf{S} - \mathbf{D} \rangle.$$

Since (36) is strongly convex with respect to  $\mathbf{w}$  and  $\mathbf{S}$  is uniquely determined by  $\mathbf{w}$ , thus (36) admits a unique solution, denoted by  $(\bar{\mathbf{w}}, \bar{\mathbf{S}})$ . By the Slater's condition and  $\mathbf{X}_* \in \mathcal{X}_*$ , the point  $(\bar{\mathbf{w}}, \bar{\mathbf{S}}, \mathbf{X}_*)$  satisfies the KKT equations:

$$(37) \quad 0 = \bar{\mathbf{w}} - \mathbf{b} + \mathcal{A}(\mathbf{X}_*), \quad 0 \in \mathbf{X}_* + \mathcal{N}_{\mathcal{S}_+^N}(\bar{\mathbf{S}}), \quad 0 = \mathcal{A}^H(\bar{\mathbf{w}}) + \bar{\mathbf{S}} - \mathbf{D}.$$

Combining the first and the last equalities in (37), we know  $\bar{\mathbf{S}} = (\mathcal{A}^H(\mathcal{A}(\mathbf{X}_*) - \mathbf{b})) + \mathbf{D} = \nabla f(\mathbf{X}_*)$ . It is from (17) and the Proposition 3.2 in [12] that  $\text{rank}(\mathbf{X}_*) + \text{rank}(\bar{\mathbf{S}}) = N$ . Then, applying the Corollary 3.1 in [12], we obtain that for any  $\bar{\mathbf{X}} \in \mathcal{X}_*$ ,  $\partial h$  is metrically subregular at  $\bar{\mathbf{X}}$  for 0.

**Appendix D. Proof of Theorem 4.3.** We first present a lemma that establishes the relationship between metric sub-regularity of  $\partial h$  and the KL inequality at critical points.

**Lemma D.1.** *Let  $h = f + g$  be defined as they are in (9) and assume  $\mathcal{X}_* \neq \emptyset$ . If  $\partial h$  is metrically subregular at  $\bar{\mathbf{X}}$  for  $\mathbf{0}$ , then  $h$  satisfies the KL inequality at  $\bar{\mathbf{X}}$  with  $\phi(x) = c\sqrt{x}$  for some  $c > 0$ .*

*Proof.* Since  $h$  is convex, we know  $\mathcal{X}_* = \partial h^{-1}(\mathbf{0})$ . If  $\partial h$  is metrically subregular at  $\bar{\mathbf{X}}$  for  $\mathbf{0}$ , then there exist  $\kappa$  and  $\epsilon > 0$  such that

$$(38) \quad \text{dist}(\mathbf{X}, \mathcal{X}_*) = \text{dist}(\mathbf{X}, \partial h^{-1}(\mathbf{0})) \leq \kappa \text{dist}(\mathbf{0}, \partial h(\mathbf{X})), \quad \forall \mathbf{X} \in \mathbb{B}(\bar{\mathbf{X}}, \epsilon).$$

Thus, for any  $\mathbf{X} \in \mathbb{B}(\bar{\mathbf{X}}, \epsilon) \cap [h(\mathbf{X}) > h(\bar{\mathbf{X}})]$ , we have

$$(39) \quad h(\mathbf{X}) - h(\bar{\mathbf{X}}) = h(\mathbf{X}) - h(\mathbf{X}_*) \leq \|\mathbf{U}\|_{\mathbb{F}} \|\mathbf{X}_* - \mathbf{X}\|_{\mathbb{F}}, \quad \forall \mathbf{X}_* \in \mathcal{X}_*, \quad \forall \mathbf{U} \in \partial h(\mathbf{X}),$$

where the inequality is a consequence of the convexity of  $h$  and the Cauchy-Schwartz inequality. Taking the infimum over all  $\mathbf{X}_* \in \mathcal{X}_*$  and over all  $\mathbf{U} \in \partial h(\mathbf{X})$  in (39) and then using (38), we have

$$h(\mathbf{X}) - h(\bar{\mathbf{X}}) \leq \kappa \text{dist}(\mathbf{0}, \partial h(\mathbf{X}))^2,$$

which implies  $h$  satisfies the KL property with  $\phi(x) = 2\sqrt{\kappa x}$ . ■

Now, inspired by the analysis in [2], we are ready to present the proof for [Theorem 4.3](#).

*Proof.* Let  $\bar{\mathbf{X}} \in \mathcal{X}_*$  such that  $\lim_{k \rightarrow +\infty} \mathbf{X}_k = \bar{\mathbf{X}}$ . Assume that  $h(\mathbf{X}_k) > h(\bar{\mathbf{X}})$  for all  $k$ . Otherwise, by the decrease property (23), it is easy to know  $h(\mathbf{X}_k) = h(\bar{\mathbf{X}})$  and  $\mathbf{X}_k = \bar{\mathbf{X}}$  for all  $k > k_0$  whenever  $h(\mathbf{X}_{k_0}) = h(\bar{\mathbf{X}})$ . Define  $r_k = h(\mathbf{X}_k) - h(\bar{\mathbf{X}})$ . The fact that  $\mathbf{X}_k \rightarrow \bar{\mathbf{X}}$  as  $k \rightarrow +\infty$  combined with [Proposition 4.2](#) and [Lemma D.1](#) establishes the existence of some  $k_\ell > 0$  such that the following inequality holds:

$$(40) \quad h(\mathbf{X}_k) - h(\bar{\mathbf{X}}) \leq \kappa \text{dist}(\mathbf{0}, \partial h(\mathbf{X}_k))^2, \quad \forall k > k_\ell.$$

Applying (24) and (23) to (40), we obtain that

$$(41) \quad \begin{aligned} r_k &\leq \kappa b^2 (\|\mathbf{X}_k - \mathbf{X}_{k-1}\|_{\mathbb{F}} + \bar{w} \|\mathbf{X}_{k-1} - \mathbf{X}_{k-2}\|_{\mathbb{F}})^2 \\ &\leq 2\kappa b^2 \left( \|\mathbf{X}_k - \mathbf{X}_{k-1}\|_{\mathbb{F}}^2 + \bar{w}^2 \|\mathbf{X}_{k-1} - \mathbf{X}_{k-2}\|_{\mathbb{F}}^2 \right) \\ &\leq 2\kappa a^{-1} b^2 \left\{ F(\mathbf{X}_{k-1}) - F(\mathbf{X}_k) + \bar{w}^2 [F(\mathbf{X}_{k-2}) - F(\mathbf{X}_{k-1})] \right\} \\ &= c(r_{k-1} - r_k + \bar{w}(r_{k-2} - r_{k-1})) \end{aligned}$$

where  $c = 2\kappa a^{-1} b^2$  and the second inequality is from the geometric inequality. Since  $r_k \leq r_{k-1}$  for all  $k$ , the inequality (41) implies

$$r_k \leq \frac{c}{1+c} \left[ (1-\bar{w})r_{k-1} + \bar{w}r_{k-2} \right] \leq \frac{cr_{k-2}}{1+c} \leq r_{k_\ell} \left( \frac{c}{1+c} \right)^{\frac{k-k_\ell-1}{2}}, \quad \forall k > k_\ell.$$

Furthermore, using (34), for all  $\hat{k} > k > k_\ell$ , we have

$$(42) \quad \begin{aligned} (1-\bar{w})\|\mathbf{X}_{\hat{k}} - \mathbf{X}_k\|_{\mathbb{F}} &\leq (1-\bar{w}) \sum_{i=k}^{\hat{k}-1} \|\mathbf{X}_{i+1} - \mathbf{X}_i\|_{\mathbb{F}} \\ &\leq (1+\bar{w}) \sum_{i=k-2}^k \|\mathbf{X}_{i+1} - \mathbf{X}_i\|_{\mathbb{F}} + b\sqrt{r_k}/a \\ &\leq (1+\bar{w}) \sum_{i=k-2}^k \sqrt{\frac{h(\mathbf{X}_{i+1}) - h(\mathbf{X}_i)}{a}} + b\sqrt{r_k}/a \leq \tilde{\nu} \sqrt{r_{k-2}} \end{aligned}$$

where  $\tilde{\nu} = (1+\bar{w})\sqrt{2/a} + b/a$ . Letting  $\hat{k} \rightarrow +\infty$  in (42), we thus know that for all  $k > k_\ell + 2$

$$(43) \quad \|\mathbf{X}_k - \bar{\mathbf{X}}\|_{\mathbb{F}} \leq \nu \sqrt{r_{k_\ell}} \left( \frac{c}{1+c} \right)^{\frac{k-k_\ell-3}{4}},$$

where  $\nu = (1-\bar{w})^{-1} \tilde{\nu}$ . ■